GASTROINTESTINAL SEGMENT TRACKING OF INGESTIBLE CAPSULES USING BIODEGRADABLE SUPERSTRATES

by

Azar Hadi

B.S., Electrical and Electronics Engineering, Urmia University of Technology, 2015

Submitted to the Institute for Graduate Studies in
Science and Engineering in partial fulfillment of
the requirements for the degree of
Master of Science

Graduate Program in Elactrical and Electronics Engineering
Boğaziçi University

2024

GASTROINTESTINAL SEGMENT TRACKING OF INGESTIBLE CAPSULES USING BIODEGRADABLE SUPERSTRATES

APPROVED BY:

Assoc. Prof. Sema Dumanlı Oktar (Thesis Supervisor)	.....
Assoc. Prof. Ahmet Öncü	.....
Assist. Prof. Zeliha Cansu Canbek Özdil	.....

DATE OF APPROVAL: 06.08.2024

ACKNOWLEDGEMENTS

First and foremost, I want to express my deepest gratitude to my advisor, Assoc. Prof. Dr. Sema Dumanlı Oktar, whose guidance, exemplary dedication, and patience have made this work possible. Working under her mentorship has been a profoundly enlightening experience. She has been a guiding beacon on my path.

I extend my gratitude to my lab mate, Burak Ferhat Özcan. The time and effort he spent during our experiments helped me become proficient in conducting experiments.

Many thanks to Dr. Denys Nikolayev and Erdem Çil from Université de Rennes for providing us with the ingestible capsule. This contribution was instrumental in validating our methodology through experiments.

I am grateful to Assist. Prof. Dr. Zeliha Cansu Canbek Özdil and Elif Sümeyye Cirit from Yeditepe University for their contribution to our project through their work on capsule coatings. Their collaboration made our experiments possible.

BOUNtenna, a place that nurtures learning and growth, has given me heart-warming moments to remember and cherish during my time at Boğaziçi University. I sincerely appreciate everything it has added to my personal and professional development. Every member of this team has taught me something valuable, and I feel incredibly lucky to have been a part of it. I thank my professor for creating and nurturing this space.

I want to express my deepest appreciation to my mother, Afsaneh Ojaghi, whose unwavering belief in me has been my strength; my father, Enayat Hadi, who always pushed me to aim higher; and my younger brother, Kousha Hadi, a wise supporter beyond his years. Their support has been instrumental to the success of this work, and

I cherish their presence deeply.

My uncle, Akbar Ojaghi, deserves my deepest gratitude for his unwavering support, which has strengthened me at every step.

ABSTRACT

GASTROINTESTINAL SEGMENT TRACKING OF INGESTIBLE CAPSULES USING BIODEGRADABLE SUPERSTRATES

Ingestible capsules can access parts of the gastrointestinal tract that are otherwise difficult to reach. The real-time and continuous data transfer from inside the gastrointestinal tract to an external reader becomes even more valuable when the reader also has spatial information about the received data. Despite valuable advancements in ingestible microelectronics technology, the tracking and localization of these devices remain an open area of research. This work aims to present a methodology that can be easily adapted to any type of ingestible capsule to track its location within the digestive tract. The novelty of this technique lies in the use of natural biodegradation as a sensing mechanism and leveraging the intrinsic electrochemical characteristics of each organ to achieve its mission. Biodegradable pH-sensitive polymers are used as coating material for an ingestible capsule with an embedded antenna. Three layers of coatings are applied around the surface of the capsule, each soluble only in one of the three target organs: the stomach, small intestine, and large intestine. As the capsule arrives in the stomach, the first layer dissolves in the acidic pH range of this tissue. This removal of one layer shifts the resonance frequency of the antenna from its initial state upon entering the digestive tract. This frequency shift indicates the capsule's presence in the stomach. The same scenario applies as the capsule transitions from the stomach to the small intestine, and from there to the large intestine. Electromagnetic simulations are presented. Based on the numerical results, electromagnetic measurements on electrochemical phantoms mimicking the dielectric properties and pH of each organ are conducted as proof of concept

ÖZET

BİYOBOZUNUR ÜSTTAŞ KULLANARAK YUTULABİLİR KAPSÜLLERİN GASTROİNTESTİNAL SEGMENT TAKİBİ

Yutulabilir kapsüller, gastrointestinal sistemin erişilmesi zor bölgelerine ulaşabilir. Gastrointestinal sistemin içinden dış okuyucuya gerçek zamanlı ve sürekli veri aktarımı, okuyucunun aynı zamanda alınan veriler hakkında mekansal bilgiye sahip olması durumunda daha da değerli hale gelir. Yutulabilir mikroelektronik teknolojisindeki önemli ilerlemelere rağmen, bu cihazların izlenmesi ve konumlandırılması hala araştırma alanında açık bir konudur. Bu çalışma, herhangi bir tür yutulabilir kapsüle kolayca uygulanabilecek bir konum izleme metodolojisi sunmayı amaçlamaktadır. Bu tekniğin yeniliği, doğal biyobozunmayı bir algılama mekanizması olarak kullanması ve her organın içsel elektrokimyasal özelliklerini kullanarak görevini gerçekleştirmesidir. Gömülü antene sahip yutulabilir bir kapsül için kaplama malzemesi olarak biyobozunur pH-duyarlı polimerler kullanılmıştır. Kapsül yüzeyine her biri sadece üç hedef organdan birinde çözünebilen üç katman kaplama uygulanır: mide, ince bağırsak ve kalın bağırsak. Kapsül mideye ulaştığında, ilk katman bu dokunun asidik pH aralığında çözülür. Bu katmanın çıkarılması, sindirim kanalına girerken antenin rezonans frekansını başlangıç durumundan kaydırır. Bu frekans kayması, kapsülün midede bulunduğunu gösterir. Aynı senaryo, kapsül mideden ince bağırsağa ve oradan kalın bağırsağa geçtiğinde de geçerlidir. Elektromanyetik simülasyonlar sunulmuştur. Sayısal sonuçlara dayanarak, her organın dielektrik özelliklerini ve pH'ını taklit eden elektrokimyasal fantomlar üzerinde elektromanyetik ölçümler kavram kanıtı olarak yapılmıştır.

TABLE OF CONTENTS

LIST OF FIGURES

LIST OF TABLES

LIST OF SYMBOLS

a	Dipole radius
c	Speed of light in free space
f	Frequency in Hertz
f_c	Center frequency
$\mathrm{I_e}$	Dipole current distribution
I_0	Current maximum
I_{in}	Input current
l	Dipole length
k	Wave number
$\lvert S_{11}\rvert$	Magnitude of the reflection coefficient
$\angle S_{11}$	Phase of the reflection coefficient
R_{in}	Input resistance
R_r	Radiation resistance
X_m	Input reactance
Z_w	Wave impedance
ε_0	Permittivity of free space
ε_r	Relative permittivity
η	Intrinsic impedance
λ	Wavelength
λ_0	Wavelength in free space
λ_g	Guided Wavelength
σ	Conductivity
Ω	Ohm
$\varnothing$	Diameter

LIST OF ACRONYMS/ABBREVIATIONS

3D	Three Dimensional
ADC	Analog to Digital Converter
ATRP	Transfer Radical Polymerization
CCMDA	Conformal Chandelier Meandered Dipole Antenna
CE	Capsule Endoscopy
CT	Computerized Tomography
DOF	Degrees of Freedom
DoA	Direction of Arrival
EM	Electromagnetic
FDA	Food and Drug Administration
FDTD	Finite-Difference Time Domain
Fe	Iron
FEM	Finite Element Method
GI	Gastrointestinal
HFSS	High-Frequency Structure Simulator
ICP	Intracranial Pressure
ISM	Industrial Scientific Medical
LIOP	Local Intensity Order Pattern
Mg	Magnesium
MICS	Medical Implant Communication Service
MLDA	Meandered Line Dipole Antenna
Mo	Molybdenum
MSER	Maximally Stable Extremal Regions
NB	Narrow Band
PAN	Personal Area Networks
PCB	Printed Circuit Board
PCL	polycaprolactone
PD	Personal Device

PGA	polyglycolide
PGS	poly(glycerol sebacate)
PHA	polyhydroxyalkanoates
PHB	polyhydroxybutyrate
PHV	polyhydroxyvalerate
PLA	polylactide
PLGA	poly(lactic-co-glycolic acid)
PLLA	poly(L-lactic acid)
POMaC	poly[octamethylene maleate (anhydride) citrate]
POC	poly(1,8-octanediol-co-citrate)
PPy	polypyrrole
PU	polyurethanes
pSi	Porous silicon
PSS	poly(styrene sulfonate)
PVA	polyvinyl alcohol
RAFT	Reversible Addition–Fragmentation chain Transfer
RF	Radio Frequency
RSS	Received Signal Strength
SIFT	Scale-Invariant Feature Transform
Si-NM	Silicon Nanomembrane
SiO_2	Silicon dioxide
Si_3N_4	Silicon nitride
SLDA	Single Line Dipole Antenna
SURF	Speeded Up Robust Features
TLM	Transmission Line Model
ToA	Time of Arrival
UWB	Ultra Wide Band
UV	Ultra Violet
VCE	Video Capsule Endoscopy
VHF	Very High Frequency
W	Tungsten

WBAN	Wireless Body Area Networks
WCE	Wireless Capsule Endoscopy
Zn	Zinc

1. INTRODUCTION

1.1. The Question

By the late 20th century, advancements in electronics had led to the miniaturization, reduced power consumption, and also cost-efficiency of electronic instruments, enabling a new era of wireless networks. This evolution enabled the creation of wireless networks operating within short distances, including those confined to an individual's immediate vicinity. Addressing the need for information exchange among devices placed on or near the human body, Thomas Guthrie Zimmerman introduced the concept of Personal Area Networks in his 1995 thesis titled "Personal Area Networks (PAN): Near-Field Intra-Body Communication." Zimmerman utilized near-field electrostatic coupling to establish the operation of such networks [1]. PANs laid the groundwork for Wireless Body Area Networks (WBANs), designed to function on or within the human body.

In response to the burgeoning research in the WBAN domain, the IEEE Standards Association established the IEEE 802.15 Task Group 6 in 2007. This task group is dedicated to developing a communication standard optimized for low-power devices, designed to operate on, in, or around the human body [2]. A WBAN comprises small, intelligent devices such as sensors, actuators, and Personal Devices (PDs), functioning on or within the human body. These devices facilitate real-time and continuous monitoring of physiological data, which can be accessed by users or healthcare professionals. In-body sensors detect physiological stimuli and wirelessly transmit the collected data [3]. Actuators, functioning as control units, respond to this sensor data or user inputs to manipulate environmental interactions [4]. PDs relay information from sensors and actuators to the user. WBANs enable these interactions and find extensive applications in medical and non-medical fields.

Non-medical applications of WBANs include real-time streaming, entertainment, emergency services, motion detection, and secure authentication [5]. However, this discussion will specifically focus on the medical applications of WBANs, which are explored in greater detail.

WBANs hold significant potential to transform healthcare monitoring by enabling the diagnosis of life-threatening diseases and facilitating real-time patient monitoring [6]. Advancements in micro-electronic miniaturization, sensor technology, the Internet, and wireless networking aim to fundamentally transform and modernize healthcare services. The implementation of WBANs is anticipated to enhance healthcare systems by improving the management and detection of illnesses and facilitating proactive responses to medical crises beyond mere wellness monitoring [7, 8]. The medical applications of WBANs are broadly categorized into three main types: wearable, implantable, and remote management of medical instruments [5]. For this study, we focus primarily on implantable WBANs, while the discussion of wearable WBANs and remote management of medical instruments is beyond the scope of this work.

Implantable WBANs play a critical role in managing various health conditions such as ocular diseases, cochlear damage, tumors, and cardiovascular diseases, as well as facilitating drug delivery. They also offer particular advantages in diagnosing and monitoring the gastrointestinal (GI) tract, where restricted access presents unique challenges for healthcare providers [9]. The GI tract can provide valuable physiological insights about nearly entire human body [10]. Some medical conditions involving the GI tract include dysphagia, gastroparesis, and irritable bowel syndrome [11].

Invasive medical interventions, such as endoscopic examination and manometric evaluation, or approaches that demand frequent exposure to possibly dangerous X-ray radiation, including computerized tomography (CT) and scintigraphy, are currently employed for monitoring GI tract [10, 12–15]. Ultrasound is another method used for this purpose [16]. These practices necessitate constant evaluations in a healthcare facility. This can complicate monitoring due to the limited motility of the patient [17].

Ingestible electronics enable the temporary and noninvasive implantation of sensors within the body. Currently, various ingestible technologies are used to detect and visualize GI tract anomalies during standard screening procedures. Developing ingestible electronic sensors as diagnostic tools or drug delivery systems carries the potential to enhance or decentralize medical services by autonomously collecting data. This data can then be analyzed and interpreted by secondary data management systems and transmitted to a medical team. These tools can be configured for use at any desired time interval [10]. The PillCam series marketed by Medtronic, is an example of Food and Drug Administration (FDA)-approved ingestible electronics [10].

Wireless motility capsules and video capsule endoscopy (VCE) are instances of this technology which offer the ability to monitor the GI tract without interfering with daily activities [18–23]. Wireless motility capsules are designed to be ingested to monitor pH, pressure, and temperature throughout the GI tract, while VCEs are equipped with video capture functionality. However, these methods do not directly measure the capsule's placement within the GI tract; instead, location must be deduced from the gathered data, allowing for organ mapping at a broad scale [17]. Despite significant advancements in wirelessly controlled ingestible bioelectronics, a major challenge remains in accurately determining the capsule's whereabouts within the GI tract [24].

1.2. Organization of the Thesis

Chapter 1 introduces the concept and objectives of the proposed work. Chapter 2 provides an extensive literature review for this multidisciplinary work and highlights the novelty of the proposed system. Thesis considerations are explored in Chapter 3. Chapter 4 presents the numerical models of the proposed sensing system, including both mechanical and electromagnetic analyses. Chapter 5 describes a measurement setup using GI tract-mimicking phantoms and discusses the measurement results. Chapter 6 concludes the work, and Chapter 7 explores possible directions for future research.

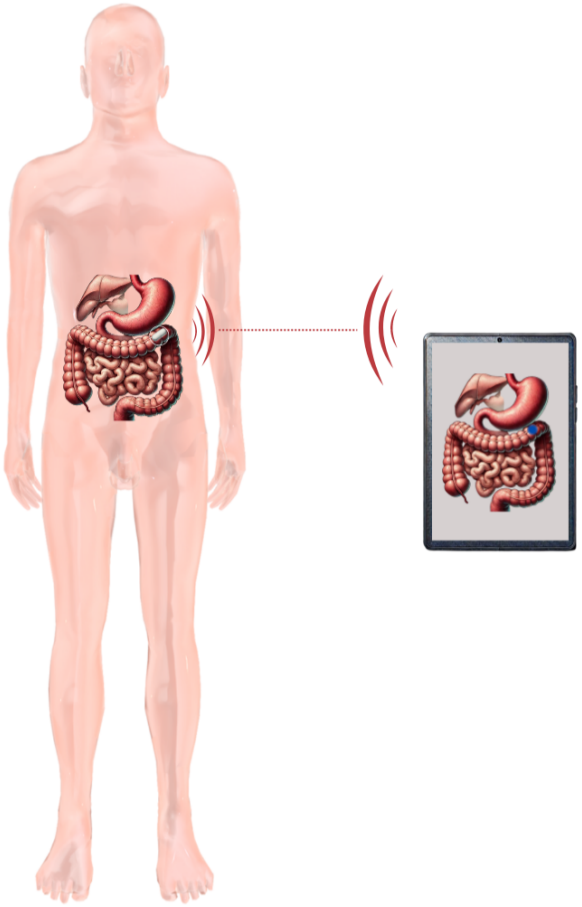

Figure 1.1. PD tracking an ingestible capsule.

2. LITERATURE REVIEW

Real-time monitoring of wireless microelectronic devices within the GI tract offers significant advantages across medical applications. It enables spatially accurate anatomical sensing, facilitating targeted drug delivery to specific areas for enhanced treatment efficacy. This capability also promotes medication adherence monitoring, ensuring patients follow prescribed regimens accurately. Moreover, real-time tracking supports selective electrical stimulation for therapeutic purposes and provides precise disease localization, which is crucial for guiding surgical interventions. A three-dimensional anatomical map of the GI tract aids in pre-surgical preparation, providing surgeons with detailed insights and facilitating minimally invasive procedures, which reduce risks and enhance recovery times [10,12–14]. Continuous monitoring of GI transit times is particularly essential for diagnosing and managing GI motility disorders such as gastroparesis, ileus, and constipation, which are prevalent in conditions like diabetes mellitus and inflammatory bowel disease [17]. Real-time tracking provides invaluable insights into these disorders, ultimately advancing patient care and improving quality of life for affected individuals.

Section 2.1, provides a literature review of tracking methods for ingestible devices. Section 2.2 reviews available work on ingestible pH sensors, and finally, Section 2.3 offers a literature review of biodegradable sensors, focusing on the material aspects of their design.

2.1. Tracking Ingestible Devices

In recent years, numerous studies have focused on developing precise localization systems for ingestible capsules. These studies can be categorized in four general groups [25]:

- Radio Frequency (RF)-based

- Magnetic-based
- Video-based
- Other techniques

RF localization techniques aim to use an RF signal to communicate information with an external reader [25] and consider measuring one or more parameters of the received signal, such as Received Signal Strength (RSS), Time of Arrival (ToA), and Direction of Arrival (DoA) [26]. One major challenge in RF-based localization is the significant attenuation of RF signals within the human body [27].

The RSS method is the most commonly utilized technique. It involves converting the received signal into a distance measurement between the capsule and sensors located on the body surface. The position of the capsule can then be estimated using approximation or estimation algorithms [28].

The localization and tracking of Wireless Capsule Endoscopy (WCE) within the intestines are explored in [29]. Localization is achieved using the RSS method through electromagnetic simulations on a human model, with Kalman and particle filters used for tracking. The study found that narrowband (NB) signals reduce estimation errors in the RSS technique compared to ultra-wideband (UWB) signals. Due to dissatisfaction with localization accuracy, datasets were used instead of relying solely on RSS-based position measurements. The Kalman filter demonstrated a minimal error of just a few millimeters in detecting traveled distances, even amidst significant noise. However, the validity of this model is questioned due to the limited availability of realistic data. Additionally, the analysis did not consider the stomach.

[30] explores RSS-based localization techniques in the UWB frequency range through laboratory measurements with customized multilayer phantoms and in vivo experiments using data from a recent living pig study. The research highlights the critical role of the path loss model in accurately localizing ingestible capsules. The study notes that the model becomes invalid if the distance between the capsule and

the receiver antenna outside the body exceeds 8 cm. Additionally, the model assumes a constant orientation for the capsule, which can significantly impact accuracy in realistic scenarios since the capsule's orientation changes during its travel within the GI tract due to peristaltic movements.

In [31], both RSS and TOA methods were used to localize a WCE. The RSS method resulted in a localization error of 5 cm, while the TOA method achieved an error of 1.5 cm. However, achieving this level of accuracy required the placement of 32 sensors on the body, which significantly hinders patient mobility in practical scenarios.

Although RF-based localization techniques within the Medical Implant Communication Service (MICS) band have been extensively researched [24, 28, 32], there is still limited research on techniques using the UWB frequency band; in-body to on-body telemetry requires a standardized channel model at the operating frequency to accurately calculate signal attenuation for localization. This absence of standardized models poses a significant challenge for RF-based localization techniques. For example, UWB signals, which are beneficial for in-body microelectronic devices due to their low power consumption, necessitate further research to establish a standard channel model [25].

Magnetic localization approaches involves locating a magnet as it travels through the GI tract with an external set of magnetic sensors [33–37]. The advantage of magnetic field-based localization lies in its minimal interaction with the human body. Static and quasi-static magnetic fields can penetrate body tissue without any significant attenuation. Moreover, magnetic tracking is non-line-of-sight, enabling capsules to be detected without requiring direct visibility to magnetic sensors. Literature consistently reports that magnetic-based localization generally achieves superior accuracy compared to video and RF-based methods, highlighting its efficacy in navigating the complexities of the GI tract [24].

[17] presents a novel system for real-time, millimeter-scale localization and tracking of ingestible microdevices within the GI tract. The technology utilizes three-dimensional magnetic field gradients generated by planar electromagnetic coils to encode spatial locations, allowing wireless devices to transmit their position with high accuracy. This system aims to improve the diagnosis and treatment of GI disorders, offering non-invasive, continuous monitoring in real-world settings without harmful radiation. Key advantages include high spatial resolution, wireless operation, and the ability to track multiple devices simultaneously, promising applications in GI motility analysis, targeted drug delivery, and surgical planning. [35] presents a five-dimensional localization technique for a meso-scale magnetic robot controlled via a computer-operated electromagnetic system. The method uses a two-dimensional array of mono-axial Hall-effect sensors to measure perpendicular magnetic fields, enhancing the accuracy of robot localization. Two key steps are involved: first, the magnetic field of the electromagnet is subtracted from the measured data to isolate the robot's magnetic field. Then, this subtracted field undergoes second-order differentiation in the perpendicular direction to minimize the electromagnetic field's impact on localization. Through optimization, the robot's position and orientation are determined with a positional error of 2.1 ± 0.8 mm and an angular error of $6.7\pm4.3^\circ$ within a 5 cm range at 200 Hz. [38] introduces IM6D, a magnetic motion-tracking system with small, wireless, 6-DOF markers, suitable for dexterous 3D interactions. Utilizing electromagnetic induction and an external pickup coil array, the system resolves issues like dead-angles, providing reliable tracking at reasonable speeds. Through experiments, it demonstrated its utility in complex environments like finger-tracking in occluded spaces, promising advances in virtual reality and interaction sensing.

CE, with built-in cameras, leverages image processing and machine vision techniques to track the ingestible's movement within the GI tract, as discussed in references [39–41]. A significant advantage of video-based localization is its ability to operate without additional hardware, providing a cost-effective solution. Furthermore, tracking is independent of on-body sensors typically worn around the abdomen, ensuring that patient activities do not disrupt the localization process.

Body-SLAM is a simultaneous localization and mapping technique designed for WCE within the human GI tract. This technique aims to enhance the positioning accuracy of endoscopic capsules by fusing data from visual and RF signals. The approach involves analyzing feature points between consecutive images captured by the capsule to estimate speed and orientation, integrating this data with RF measurements using a Kalman filter. The proposed method achieves an average tracking error of less than 2.3 cm, providing a reliable map of the small intestine to aid in the precise identification of intestinal diseases. This research addresses significant challenges in localizing WCEs, including the complex anatomy of the small intestine and the RF signal's behavior in non-homogeneous body tissue, as outlined in [42].

A detailed study in [43] explores methods for 3D motion estimation in WCE, a non-invasive procedure used for gastrointestinal tract inspection. The main challenge is to accurately track the capsule's movement through the GI tract using image registration between consecutive frames. The study compares several image registration techniques, including pixel-based, feature-based, and AI-based methods, using a dataset from a robotic setup with an ex-vivo porcine colon. The research finds that conventional feature-based methods like SIFT, SURF, MSER, and LIOP are inadequate for robust matching due to the GI tract's complex nature. The study concludes that a deep-learning approach, PWC-Net, yields the most accurate results, offering a promising solution for real-time 3D motion estimation in WCE.

In most video-based localization methods for CE, both simulation and experimental studies often fail to account for the peristalsis. These studies typically assume that the capsule follows a unbending path at a constant rate, which inaccurately represents the complex and periodic contractions characteristic of the GI tract. Significant limitations that affect the precision of localization with video-based techniques include the constrained image resolution and frame rate of capsule endoscopes. These limitations arise from low battery capacity and the necessity for the device to operate at low frequencies.

Currently, research into video-based localization of CE is still in its early stages. Future studies need to incorporate in vivo measurements to validate the reliability of these methods under real-world conditions and to address the dynamic and complex environment of the GI tract.

Other methods involve utilizing physical environmental parameters that vary across different regions of the gut, such as variations in oxygen and pH. By embedding oxygen and pH sensors in capsules, and analyzing their output profiles, these variations can be detected to accurately identify transitions from one organ to another [44].

2.2. Ingestible pH Sensors

[45] features ion-sensing thread-based electrochemical sensors, which are integrated onto the surface of a 3D-printed cap, along with essential readout electronics. It utilizes a polyaniline-based potentiometric pH sensing thread that generates a voltage output proportional to the detected pH level.

Very similar in principle to the [45], When ingested, the capsule system in [46] encounters hydrogen ions (H^+) from GI biofluids, which infiltrate the sensor cavity through a grid on its top. An embedded pH sensor based on iridium oxide within the capsule responds to these pH levels by generating a corresponding potential signal. This signal is captured by a potentiostat within the capsule's detection unit, which is connected to the pH sensor. The potentiostat relays this potential signal to an Analog-to-Digital Converter (ADC), transforming it into a digital voltage signal.

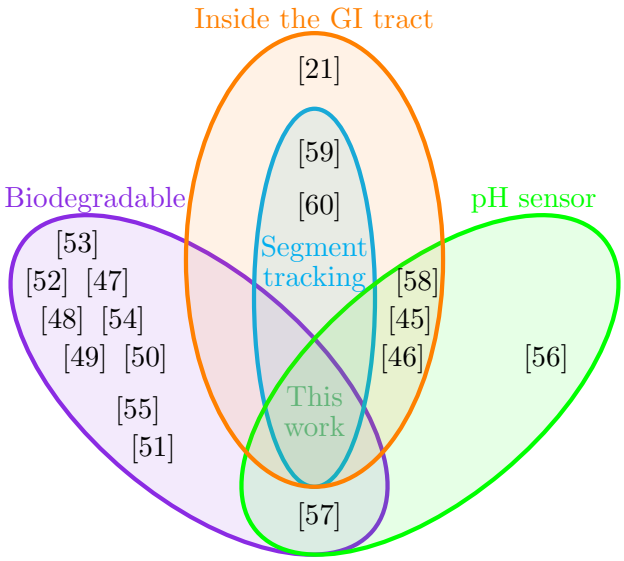

Figure 2.1. A comparison of the proposed study with related in-body sensors in the literature.

2.3. Biodegradable Sensors

The medical necessity to temporarily monitor changes in pressure, temperature, and pH in specific locations of various tissues for disease and therapy monitoring has driven the development of implantable sensors. However, these sensors often require a second operation for removal, posing a risk of tissue damage. To address this issue, the literature suggests using biodegradable implant and ingestible sensors. Biodegradable implant sensors are particularly valuable for real-time monitoring of physiological data, as they eliminate the need for complex removal procedures once the monitoring period concludes. Ingestible sensors provide a non-invasive approach and do not cause complications or foreign-body responses. Despite the promising results presented in the literature, there are no commercially available biodegradable sensors yet. Research in this area needs to expand further in a multidisciplinary manner to reach its potential for commercialization. [61].

Material candidates for biodegradable in-body sensors need to satisfy several properties, including biocompatibility, cytocompatibility, and stability over time in both structure and function. These properties ensure that the sensors can safely in-

teract with biological tissues without causing adverse reactions and maintain their integrity and performance throughout the monitoring period [62]. The ability of a material to perform with an appropriate host response in a specific situation is regarded as biocompatibility [63]. The materials should enable the device to function properly throughout its selected operational lifetime without causing any harmful reactions in the ambient tissues or any other regions of the body. This requirement ensures the safe and effective use of the sensors for their intended purpose.

A biodegradable sensor is supposed to be fully composed of biodegradable materials. These materials are typically studied under three main categories: metals, polymers, and silicon-based materials. Each category offers different properties and advantages for biodegradable sensor applications, depending on the specific requirements of the sensor and the intended use case [61]. However, to date, only a few fully biodegradable implant sensors have been presented [52].

2.3.1. Metals

The most prevalent metals used in fabrication of biodegradable sensors are magnesium (Mg), iron (Fe), tungsten (W), molybdenum (Mo), and zinc (Zn). Mg is the most popular metal for the development of implantable devices. Mg is preferred due to its high electrical conductivity, ease of processing, and rapid degradation characteristics [54]. For instance, Mg has been proposed for creating implantable temperature sensors by leveraging its temperature-dependent electrical resistance [51]. Leveraging its high energy density, Mg has been incorporated into the composition of biocompatible and biodegradable batteries [64]. These batteries offer a sustainable power source for implantable medical devices, with the added benefit of being environmentally friendly and safe for use within the body. Despite its advantageous properties, Mg has limiting characteristics as well. The accumulation of degradation byproducts, such as hydrogen gas and hydroxyl groups (OH^-), can cause toxicity effects. In vivo, these byproducts are typically eliminated through homeostasis and fluid circulation in the body, making tissues less vulnerable to toxic effects compared to cells in culture.

However, degradation byproducts need to be considered in all sensor designs, which limits the amount of Mg that can be used in a sensor. Controlling the lifespan of a sensor can help control the amount of H_2 and OH^- released at any time. One approach to overcoming some of the limitations of Mg is through the creation of alloys and nanostructured forms, which can enhance the material's properties and potentially reduce the amount of harmful byproducts released during degradation [65].

The mechanical properties of Fe make it well-suited for use in medical implants [66]. These properties include high strength and ductility, which make it suitable for applications requiring durability and structural integrity. Additionally, iron's degradation products, primarily iron ions, are naturally present in the body and can be managed by physiological processes. However, the corrosion rate of iron is generally slower compared to magnesium, which can be advantageous for long-term applications but require careful design to avoid prolonged exposure and potential accumulation of degradation products. To address the need for controlling the degradation rate of iron, researchers are exploring ways to alloy it with other elements or apply surface treatments to achieve the desired balance between longevity and biocompatibility. For example, by carefully designing a galvanic pair, researchers can fine-tune the degradation timeline, optimizing the sensor's functionality and biocompatibility for specific medical applications.

In applications where a short lifespan for the implant sensor is required, the approach of accelerating biodegradation is also applied to Zn implants. For instance, researchers have added a Zn layer to an Fe transducer of a pressure sensor to accelerate material degradation through galvanic corrosion [67]. This technique exploits the difference in electrochemical potential between zinc and iron, causing the Zn to corrode preferentially. The accelerated degradation process helps to control the lifespan of the sensor, ensuring it breaks down at a predictable rate. This approach is particularly beneficial in applications where timely sensor degradation is critical to avoid long-term tissue exposure and potential complications from accumulated degradation products.

2.3.2. Polymers

Another type of material with significant importance in biodegradable in-body sensors is biodegradable polymers. These polymers typically allow for straightforward processing [61] and offer a high degree of adjustability with regard to their chemical structure, shape, and dissolution kinetics. This tunability is achieved by adjusting inherent polymer characteristics, including molecular weight, crystal structure, chemical composition, hydrophilic or hydrophobic attributes, and erosion behaviour [68–70].

Polymeric materials exhibit promising characteristics for customizable and biodegradable microelectronics. These materials can be tailored to meet specific requirements which makes them ideal candidates for in-body devices [71]. Additionally, their biodegradability ensures that they break down harmlessly in the body, minimizing the risk of long-term adverse effects.

Protein polymers such as collagen, chitosan, silk, and gelatin, along with plant-based polymers like alginate, cellulose, and starch, are increasingly being noticed by biodegradable device manufacturers. Some of these materials are bioactive, which can produce an immunogenic response if used in certain implantable healthcare devices. However, their mechanical strength and complex structure make them challenging to use [70, 72, 73].

On the other hand, synthetic biodegradable polymers offer more precise control over the physical and chemical properties of temporary components and the devices they create. This is because these polymers are manufactured under controlled and repeatable conditions [72].

Since the introduction of the first biodegradable suture, polyglycolide (PGA), in the 1960s, there have been numerous advancements in the synthesis of biodegradable polymers. Numerous biodegradable poly(α-esters) cross-linked elastomers, such as poly(1,8-octanediol-co-citric acid) and poly(glycerol sebacate) (PGS), as well as

polycarbonates, polyphosphazenes, polyurethanes (PU), polydioxanones, and polyhydroxyalkanoates (PHA), have since been introduced [70, 74–78].

Polylactide (PLA) and its copolymers, such as poly(lactic-co-glycolic acid) (PLGA), are the most frequently seen polymeric materials in medical applications [61]. Mechanical properties of polymers can be adjusted by varying the ratio of lactic acid to glycolic acid, allowing for customization to meet specific requirements. For example, researchers have developed an encapsulation using PLA [47] or PLGA [79], where the polymer serves as the substrate [48] for the transducer. PLGA has also been utilized to secure the implantation area of the sensor [68] and electrical insulator [50] or optical fibers [68]. Additionally, Poly(L-lactic acid) (PLLA) has been used to create the transducer's packaging and as electrical insulators for metallic sensor components [52, 54]. In addition, PLLA has been combined with polypyrrole (PPy) to create conductive polymer composites for building biodegradable coil antennas [49]. A glue made from a mixture of PLLA, acetone, and chloroform has been used to seal the encapsulating layers of sensor devices. Both PLGA [80] and PLLA [54] have the FDA approval for use in biodegradable medical devices.

Based on the findings from using PLA and its copolymers, researchers have studied various biodegradable polymers as sensor encapsulants. For instance, the polyanhydride poly(buthanedithiol 1,3,5-triallyl-1,3,5-triazine-2,4,6(1H,3H,5H)-trione pentenoic anhydride) has been utilized as an organic encapsulation material [50]. Similarly, the soft polymer poly[octamethylene maleate (anhydride) citrate] (POMaC), combined with octanediol at a molar feed ratio of 3:2:5, has been proposed for sensor encapsulation [52]. POMaC has been reported as the encapsulation layer of an arterial pressure sensor [54], where its elasticity improves transmission of arterial pressure variations to the transducer. On the sensor side facing tissues, a stiffer material, polyhydroxybutyrate/polyhydroxyvalerate (PHB/PHV), was used to block interferences from surrounding tissues.

Another case of a polymeric encapsulant involves poly(1,8-octanediol-co-citrate) (POC) in a stretchable pressure sensor [81], with silk fibroin sheets used as the sensor substrate [82]. Additionally, a polymer blend based on 1,4-butanediol, adipic acid, and terephthalic acid has been used for sensor encapsulation [51]. Being optically transparent in the visible spectrum, this material allows for visual inspections while absorbing UV light to protect the transducer. Furthermore, it has a Young's modulus similar to that of muscle and cartilage tissues, making it ideal for encapsulating sensors used in these tissues.

These polymers are excellent encapsulants due to their ease of deposition on surfaces. However, their hydrophilicity makes them prone to swelling and water infiltration, which can lead to premature sensor failure due to the early degradation of internal components [68]. For instance, complete sensor encapsulation was achieved by leveraging the low melting temperature of polycaprolactone (PCL) [67]. Similarly, polyvinyl alcohol (PVA) was employed as an adhesive layer between the polymer substrate and various metals [53]. Additionally, PGS was utilized as the dielectric layer of the transducer in a capacitive pressure sensor [52–54].

All the polymers mentioned above have dielectric properties that make them suitable for electrical insulation. In addition to these, conductive polymers are also employed in biodegradable implantable devices [83]. These polymers offer several advantages for medical applications, including biocompatibility, biodegradability, and flexibility [83]. They can facilitate both electronic and ionic conduction, be tailored to exhibit specific chemical tendencies and sensing qualities, and be processed at low temperatures [84]. The van der Waals bonding in these materials enables precise and intimate interfaces with the body's electrolytes, eliminating the presence of dangling bonds or oxides [85, 86].

For example, PLLA can be customized for its crystalline structure and molecular orientation through thermal annealing and mechanical stretching, imparting piezoelectric characteristics suitable for sensors. Piezoelectric PLLA can be used in self-powered

sensors, is easily stackable into multilayers, and has a low relative perittivity [47]. By using a conductive ink made of poly(3,4-ethylenedioxythiophene):poly(styrene sulfonate) (PEDOT:PSS) and sericin protein photoresist, researchers developed an electrochemical transducer [82]. Although PEDOT:PSS is biocompatible, it is not intrinsically biodegradable, embedding it in sericin allows for controlled degradation.

2.3.3. Silicon-Based Materials

Silicon-based materials have a pivotal role in the development of biodegradable implant sensors. Silicon nanomembranes (Si-NMs) [81], including porous [50, 87] and nanostructured forms [88], thin films [89], and SiO_2 [90], are widely used examples. Although inherently stiff, these materials can be utilized as soft and flexible thin films. Thin films often necessitate a substrate, such as elastomers, with similar mechanical properties.

Si-NMs are used in various sensors, such as those measuring intracranial pressure (ICP), temperature, and pH [50]. Here, piezoelectric Si-NMs, for example, generate electrical signals to encode parameter values. Si nanoribbons replace Si-NMs for pH sensing, while nanoporous Si is added to serve as a backing substrate for pressure sensors and accelerometers. Piezoresistive Si-NMs are also employed in pressure and temperature sensors. [68, 91].

Porous silicon (pSi) is another attractive material for implantable systems. Its porosity accelerates material degradation, allowing the use of thicker substrates without changing the device's degradation time. While pSi is commonly used in nanoparticle form for drug delivery and medical imaging [92], it also shows promise in subcutaneous optical sensors [87, 93]. Surface treatments like silanization, hydrosilytation or hydrocarbonization can adjust the degradation rate to make pSi suitable for desired sensor lifespans.

Silicon dioxide (SiO_2) is often used as an encapsulation layer in biodegradable in-body sensors, providing protection from biofluids and electrical passivation due to its slow degradation rate and dielectric behaviour [91]. Unlike polymers, SiO_2 is not hydrophilic, offering a stable protection layer [50] from biofluids [91]. It can encapsulate transducer's active components [48], electrodes [81], or the whole electronic device, ensuring defect-free, fluid-resistant layers.

Silicon nitride (Si_3N_4) films and amorphous silica, are used in transducers as dielectric layers [51] and bonding layers [68], respectively. Trilayers of $SiO_2/Si_3N_4/SiO_2$ are employed in encapsulation and interlayer dielectrics for active neural interfaces [48].

3. PROPOSED WORK

Designing antennas for ingestible capsules presents unique challenges, particularly regarding the communication path. One major challenge is the detuning of the antenna's input impedance caused by the varying surrounding environment as the capsule progresses across the GI tract. The capsule encounters diverse EM and chemical properties in the stomach, small intestine, and large intestine. While some studies propose antenna designs resilient to EM changes throughout the GI tract, Erdem et al. proposed leveraging these variations for localization purposes. They demonstrated that differences in tissue EM properties alter the antenna's reflection coefficient, correlating with the capsule's location [94]. Building upon this concept, an enhanced technique is proposed, utilizing variations in both EM and chemical properties. Previous research has utilized biodegradation of resonating structures under different pH conditions for wireless pH sensing [55]. In this proposed improvement, the frequency shift of the antenna aims to be controlled by coating the capsule with three rings of pH-sensitive biodegradable superstrate.

The biodegradable superstrate is used to load the communication antenna of the capsule which is a meandered dipole antenna working within the 434 MHz Industrial, Scientific, and Medical (ISM) band. Considering the difference in pH levels along the GI tract, biodegradation of the superstrate can link the location data to the input parameters of the capsule antenna. The state of biodegradation of the superstrate in each segment causes a change in the reflection coefficient of the antenna, indicating the change of the segment. It is shown that a shift of at least 5 MHz can be created in the center frequency as the capsule advances along each segment in the tract while the capsule antenna is kept operational over the 434 MHz ISM band throughout.

As part of our work, we focused on optimizing a conformal meandered dipole antenna suited to our application and selecting a pH-dependent polymer for coating our capsule. The antenna is discussed in Section 3.1. Section 3.2 explores the use of

Eudragit polymer in our sensing mechanism.

3.1. Antenna

3.1.1. Choice of Antenna

The antenna utilized in this study is a conformal meandered dipole antenna, which is extensively examined in this section. The fundamental principles of dipole antennas are detailed in Appendix A.

In [96], our collaborators at the Université de Rennes conducted an investigation into how the impedance responses of ingestible capsule antennas are affected as they traverse different parts of the GI tract. The research focuses on two types of antennas—meandered dipole and meandered loop—designed to operate at 434 MHz, 1.4 GHz, and 2.4 GHz, which were integrated into capsules optimized for these frequencies within spherical homogeneous time-averaged GI phantoms.

Simulations were performed in three distinct phantoms representing the stomach, small intestine, and large intestine to evaluate how the varying EM properties of these tissues impact antenna performance. The results indicate that the encapsulation layer of the antennas minimizes detuning effects. This finding suggests that proper encapsulation effectively manages antenna robustness against environmental changes, allowing designers to focus more on improving antenna efficiency rather than robustness against detuning.

The study concludes that, while the encapsulation layer significantly reduces detuning, further research with more realistic models is necessary to confirm these findings. Additionally, the paper demonstrates that, compared to other scenarios studied, the meandered dipole antenna operating at 434 MHz exhibits higher efficiency.

This line of research is extended in [95], where the authors explore the feasibility of using impedance detuning of the previously designed meandered dipole antenna to track the location of ingestible capsules as they move through the GI tract. The meandered dipole antenna was selected for this study due to its well-established radiation mechanisms and near-field characteristics, which are more clearly understood than those of more complex antennas. The study focuses on detecting the capsule's location in different segments of the GI tract—such as the stomach, small intestine, and large intestine—based on changes in the surrounding EM properties.

Our work is built upon this study.

3.1.2. Dielectric Loading

Dielectric loading of a planar dipole antenna as shown in Figure 3.1 involves integrating dielectric materials near or within the antenna structure to modify its electromagnetic properties. This technique is frequently used to reduce the antenna's physical size while maintaining its resonance frequency as the resonance frequency decreases with increased effective permittivity [95].

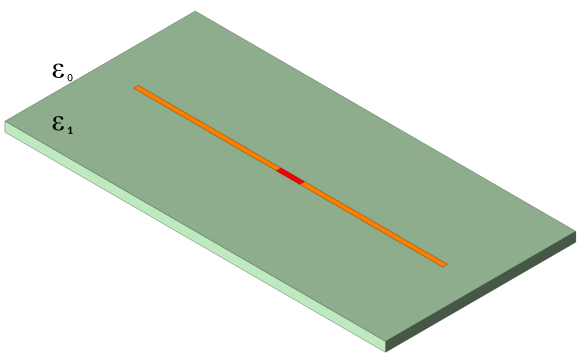

Figure 3.1. Loaded planar dipole antenna.

The determination of dipole length will then depend on the guided wavelength, as follows [96],

$$\lambda_g = \frac{\lambda_0}{\sqrt{\varepsilon_{eff}}}, \tag{3.1}$$

where,

$$\varepsilon_{eff} = \varepsilon_r \cdot ff + \varepsilon_0 \cdot (1 - ff). \tag{3.2}$$

Where ε_{eff} is called effective permittivity and represents the equivalent permittivity experienced by the electromagnetic waves propagating through both the substrate and the surrounding air. In this equation, ff represents the filling factor, quantifying the percentage of the electric fields that penetrate through the substrate. It is important to note that Equation (3.2) applies specifically when the radiating element is surrounded by only two media. In cases involving multiple complex media, the calculation becomes more complicated. Furthermore, the filling factor, ff, is likely to vary with each type of antenna and can be estimated through multiple simulations. Additionally, in a multilayered environment, where an antenna is surrounded by multiple layers of materials with different permittivities, the effective permittivity ε_{eff} can be approximated based on the distribution of the electromagnetic fields and the relative permittivities ε_r of the different layers. The exact calculation of effective permittivity can be complex and may require numerical methods, especially when the antenna operates near the interface of two media or when the media have non-uniform permittivity distributions. In such cases, techniques like the finite element method (FEM) or finite-difference time-domain (FDTD) simulations are often employed to accurately compute the effective permittivity.

This effective permittivity is crucial because it directly affects the wavelength of the waves propagating in the media, which in turn influences the antenna's resonance, impedance matching, and radiation characteristics.

The numerical and analytical data related to the dielectric loading of our antenna is discussed in Subsection 3.1.5. Prior to this, we will explore the impact of meandering and conformal designs on antenna performance, supported by examples from the literature.

3.1.3. Meandering

A difficult trade-off between frequency of operation and size specially for low-frequency applications is one of the challenges of antenna design. Due to the inverse relationship between frequency and wavelength, antennas operating in the low frequencies, can extend to several meters in length. Consequently, adapting such antennas for applications that require small dimensions is often impractical. Additionally, radiation efficiency is a concern [97]. A straight-line dipole antenna (SLDA) operates most efficiently when the imaginary part of its complex input impedance is zero, a condition met when the electrical length of each dipole leg is slightly shorter than the $\lambda/4$ at the operating frequency [98], also see Figure 3.2. As a result, practical low-frequency antennas are mostly electrically small. This means a narrow bandwidth and small radiation resistance.

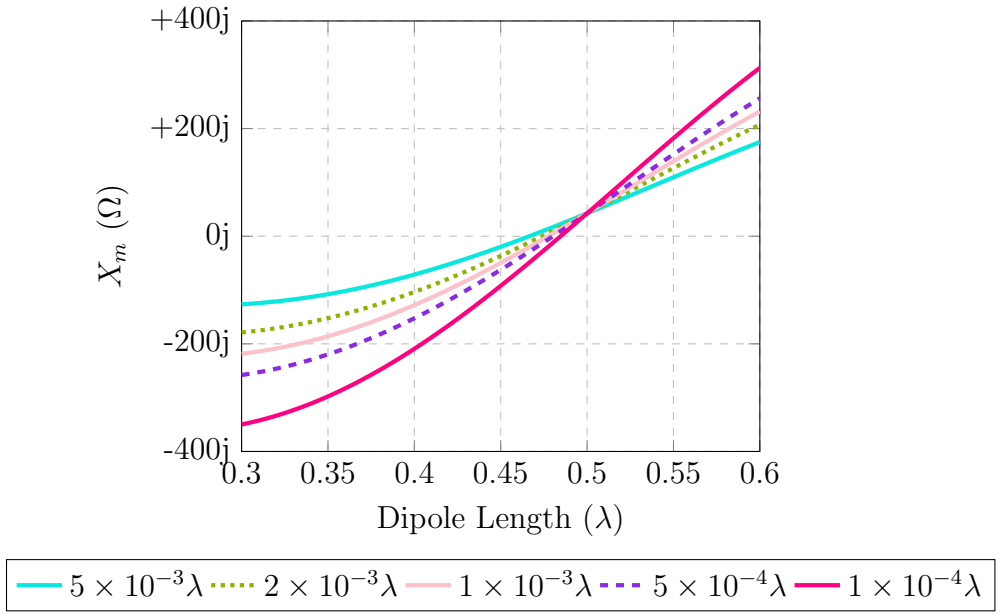

Figure 3.2. Reactance of a cylindrical dipole referred to the driving point for $a = 5 \times 10^{-3}\lambda$, $a = 2 \times 10^{-3}\lambda$, $a = 1 \times 10^{-3}\lambda$, $a = 5 \times 10^{-4}\lambda$, $a = 1 \times 10^{-4}\lambda$.

In [99] a design is used to reduce the size of linear dipole antennas by bending the radiating elements into a meander shape. A formula is derived to relate the resonant frequency to the geometric parameters of the MLDA, treating the meander portion

as an inductive load. The study also introduces a formula for calculating radiation efficiency based on the antenna's structural parameters and resonant frequency. The research demonstrates that optimal MLDA parameters can be determined to maintain desired resonant frequency and radiation efficiency, offering a practical design method for compact antennas used in portable devices. [100] proposes a new method for calculating the resonant frequency of MLDAs using a full transmission line model (TLM) approach. This method offers a straightforward way to estimate the self-resonance frequency of MLDAs by considering the antenna as a series of transmission lines, taking into account the current distribution, meander spacing, and geometrical parameters. The proposed model is compared with simulations and prototype measurements across three MLDA families, showing an error below 7.8% in all cases. The study concludes that the TLM model can effectively predict the resonant frequency and optimize meander parameters for miniaturization, making it suitable for applications in compact and low-profile wireless devices. The validity of the TLM confirms that, for a given electrical length, the length and width of bends in a meandered structure are critical in determining the resonance frequency, as they directly influence the inductance and capacitance in the equivalent TLM model. We will see this through simulations in Subsection 3.1.5.

3.1.4. Conformal Design

Conformal antennas offer several benefits for in-body applications. By adapting to the shape of the host structure, these antennas efficiently utilize available space, which is crucial in compact or densely packed environments. This capability can also be beneficial in low frequencies where there is a need to increase the antenna's electrical size. They can be integrated into the surface material, maintaining the structural integrity of the host without requiring significant modifications or reinforcements. Additionally, the conformal design helps minimize electromagnetic interference by optimally positioning the antenna relative to other electronic components. Conformal designs offer all these advantages while keeping all the benefits of antennas on rigid PCBs [101]. [102] explores the development of a specialized antenna for ingestible cap-

sule systems that transmit biological data from within the human body. The authors introduce a novel design called the Conformal Chandelier Meandered Dipole Antenna (CCMDA), which is tailored to fit the capsule's geometry and offers improved polarization diversity. The CCMDA design process begins with a planar meandered dipole, which is later adapted into a conformal structure to overcome challenges like size constraints, impedance matching, and detuning effects caused by the body's dielectric properties. Simulations and measurements demonstrate the CCMDA's ability to maintain effective radiation patterns and impedance matching at the 1.4 GHz frequency used for medical telemetry, even within the lossy environment of the human body.

[103] studied meandered loop and meandered dipole antennas for operation within the GI tract. Our work builds on the dipole design introduced in this study.

3.1.5. Conformal Meandered Dipole Antenna

The antenna is made on a 100-µm-thick Rogers CLTE-MW ($\varepsilon_r = 2.97$) substrate, conforming to the inner surface of the PLA ($\varepsilon_r = 2.7$, $\delta = 0.003$) capsule. The capsule has a shell thickness (encapsulation thickness) of 0.4 mm. The antenna design includes an offset feed to match the in-body dipole antenna to 50 Ω, accommodating the miniaturization required for in-body applications. The trace length is optimized with respect to the shell thicknesses and is equal to 14.5 mm.

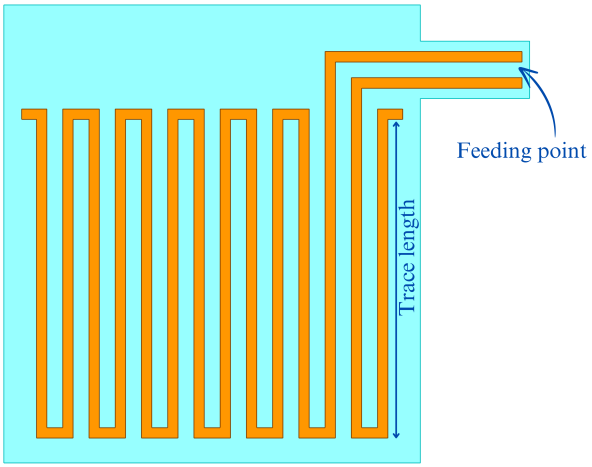

Figure 3.3. Trace length and feeding point of the original antenna.

To find the dipole length, we can start by assuming the ε_{eff} is equal to the relative permittivity of the antenna substrate, Rogers CLTE-MW, 2.97. This results in a guided wavelength that is calculated as follows,

$$\lambda_g = \frac{\lambda_0}{\sqrt{\varepsilon_{eff}}} = 412 \text{ mm}, \tag{3.3}$$

where, the wavelength λ_0 in free space is calculated as follows,

$$\lambda_0 = \frac{c}{f}, \tag{3.4}$$

where c is the speed of light in free space ($c \approx 3 \times 10^8$ meters per second), and f is the frequency in hertz.

For $f = 434$ MHz (434×10^6 Hz), λ_0 is calculated as follows,

$$\lambda_0 = \frac{3 \times 10^8 \text{ m/s}}{434 \times 10^6 \text{ Hz}} \approx 0.691 \text{ meters}. \tag{3.5}$$

Taking $\lambda_g/2$ as dipole length in order for the antenna to operate in the GI time-averaged tissue results in a resonance frequency that is higher than our desired 434 MHz due to the meandering effect. Therefore, we need to numerically tune our antenna length to reach this frequency as you can see in Figure 3.4.

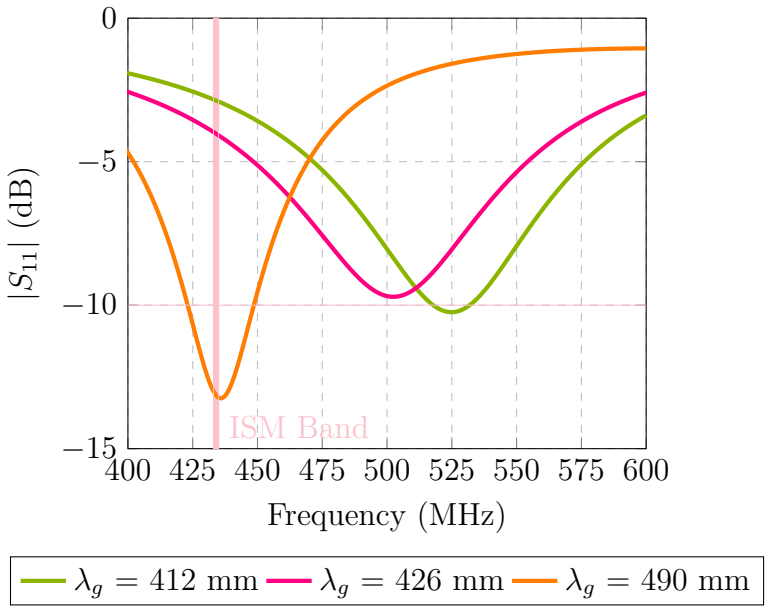

Figure 3.4. Tuning of the dipole length; PLA thickness = 0.4 mm.

Changing the PLA encapsulation thickness directly changes the ε_{eff}. In order to observe this through simulations, we changed the PLA thickness to 0.6 mm and rerun the same simulations again.

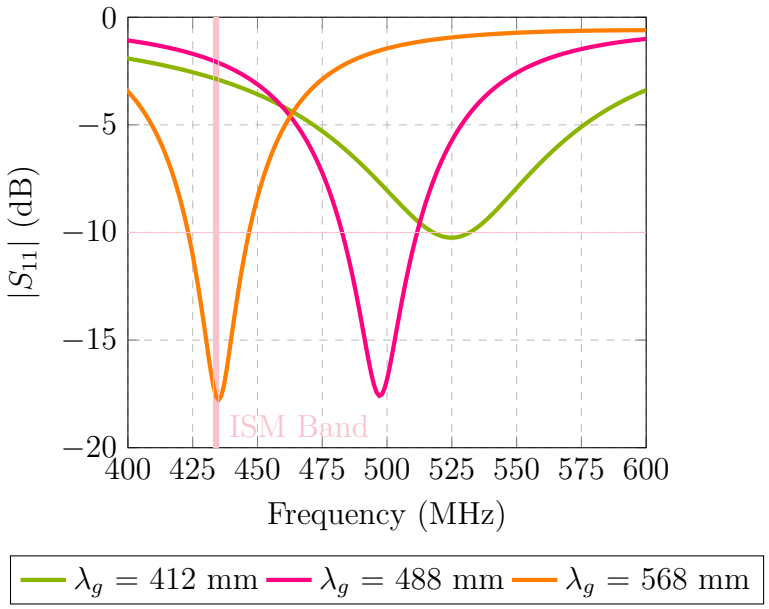

Figure 3.5. Tuning of the dipole length; PLA thickness = 0.6 mm.

Based on our numerical iterations, the optimal guided wavelength (λ_g) for 0.4 mm-thick PLA was determined to be 490 mm, with an effective dielectric constant (ε_r) of approximately 2, as calculated using Equation 3.3. For 0.6 mm-thick PLA, λ_g was found to be 568 mm, with eff approximately 1.5. These results indicate that as the thickness of PLA increases, the effective dielectric constant decreases, owing to the lower dielectric constant of PLA compared to Rogers CLT-MW. Figure 3.6 illustrates the planar model used for our simulations.

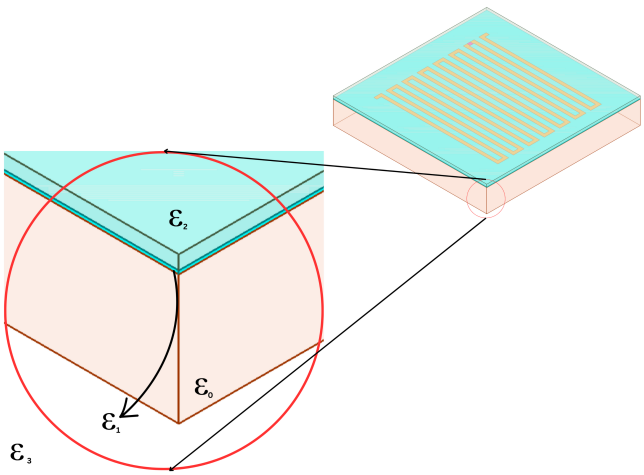

Figure 3.6. Multi dielectric loading, ε_0: air, ε_1: Rogers CLTE-MW, ε_2: PLA, ε_3: time averaged GI tract tissue.

As discussed before, meandering reduces the overall length of the antenna without affecting its resonance frequency. This is achieved by making the current path longer through the meanders, thereby keeping the electrical length similar to a straight dipole. The number of bends depends on the available physical length and in this design it is numerically set to be 7.

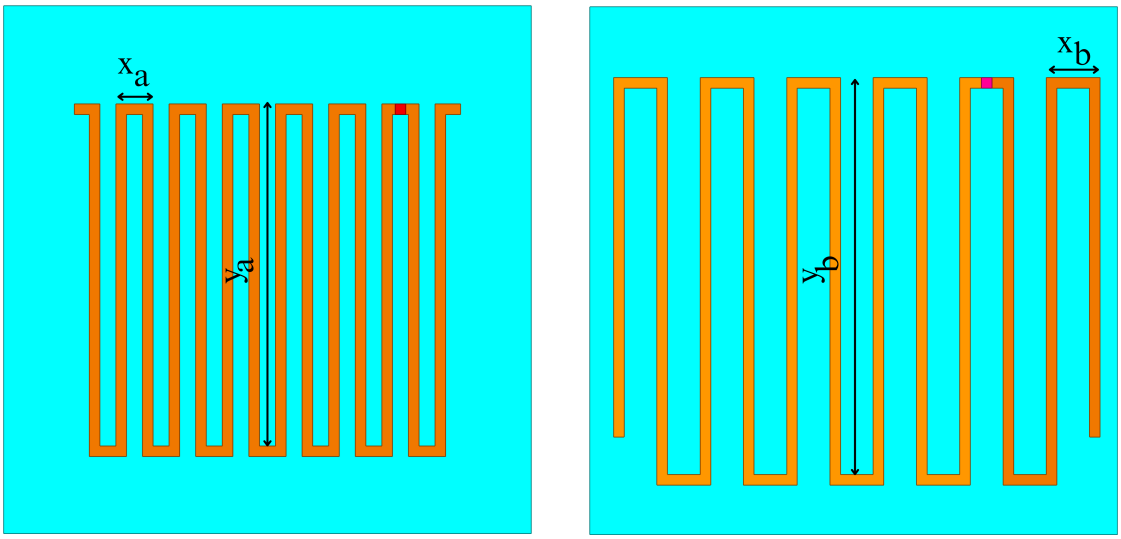

(a)

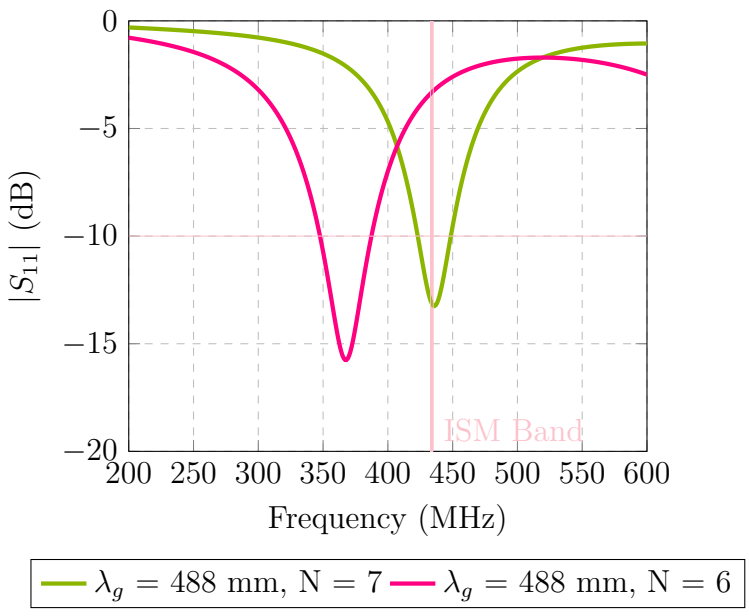

(b)

Figure 3.7. Impact of meandering (the straight unbent length is unchanged); a: $x_a = 1.76$, $y_a = 16.2$, $x_b = 2.55$, $y_b = 18.8$, b: Resonance frequency variation as a result of changing meandering size.

Another design consideration here is offset feeding which refers to a method of feeding or supplying the signal to an antenna where the feed point is not located at the center or another symmetrical point of the antenna. In the context of a dipole antenna, this means that the feed point is positioned away from the center, typically along one of the arms of the dipole. By moving the feed point away from the center,

the impedance at the feed point changes. This can be used to match the antenna's impedance with the transmission line or the feeding network, which is often desirable in practical antenna designs to achieve better power transfer and minimize reflection.

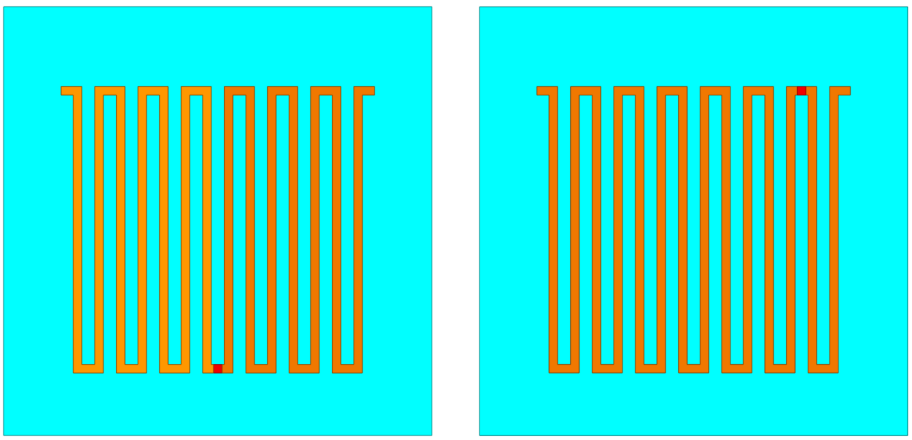

(a)

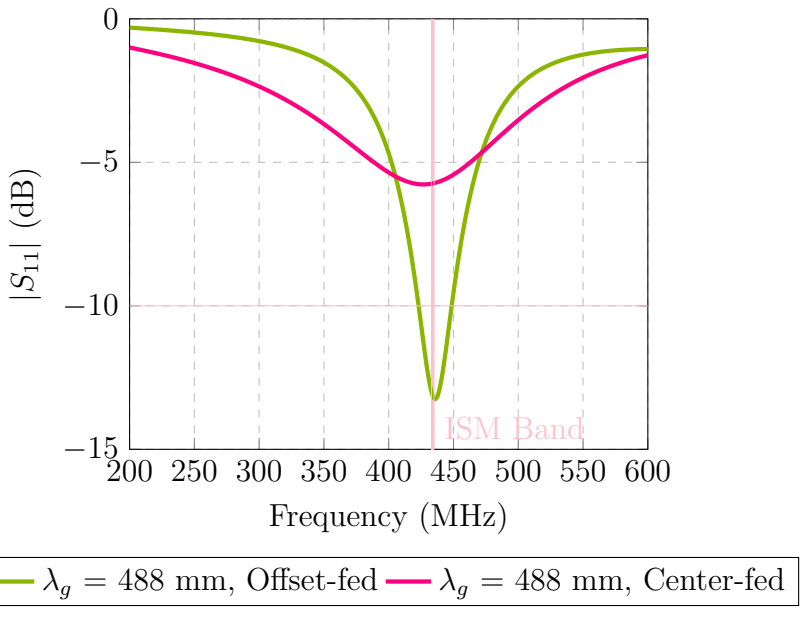

(b)

Figure 3.8. Impact of feeding; a: (Left): center-fed, (Right): offset-fed, b: Resonance frequency variation as a result of applying different feeding.

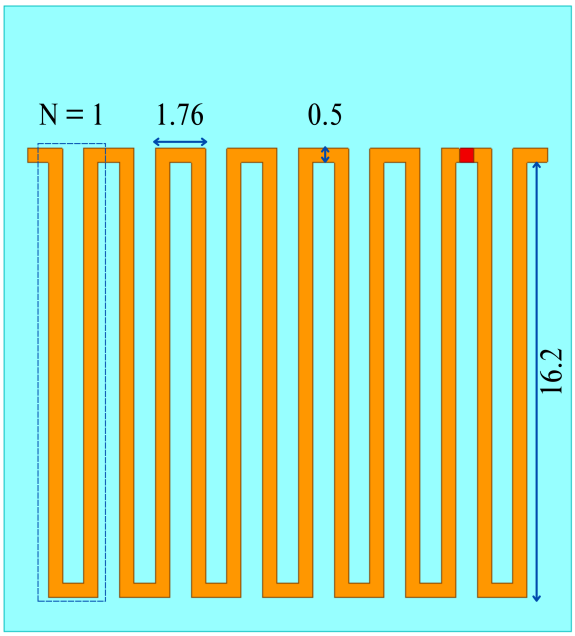

Figure 3.9. Offset-fed planar antenna (Unit: mm).

3.1.6. Optimized Design

Figure 3.11 shows the planar version of the conformal antenna used in our simulations. Coating the capsule caused a shift in the operating frequency, necessitating antenna tuning to remain within the 434 MHz ISM band. This tuning involved symmetrically extending the physical length of the dipole by 14 mm from the center. The operation of this antenna is going to be detailed in Section 4.1. Note that this subsection includes the coax-fed antenna. To feed the built-in antenna from outside the capsule, the dipole legs needed to be lengthened. This resulted in a variation of trace length between the offset-fed (16.2 mm) and coax-fed (14.5 mm) antennas to maintain the same total length.

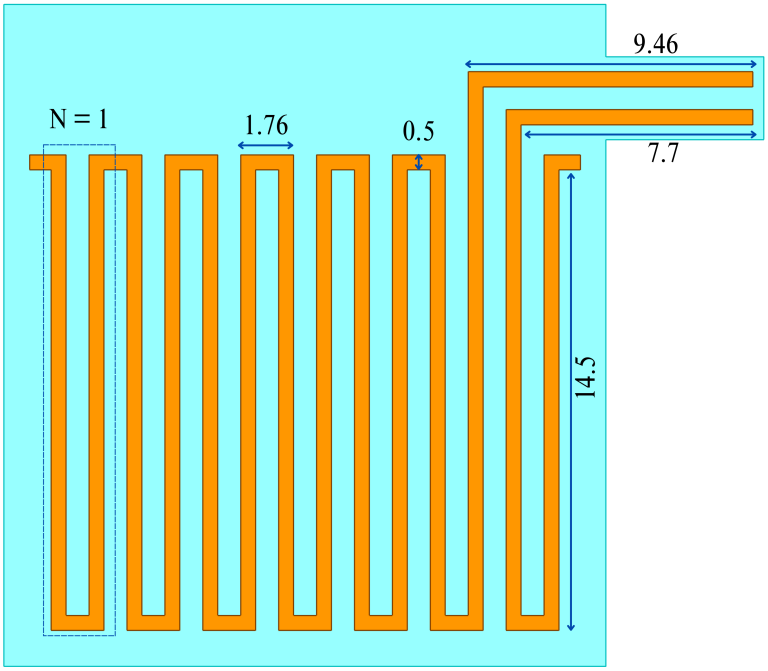

Figure 3.10. Original antenna (Unit: mm) [94].

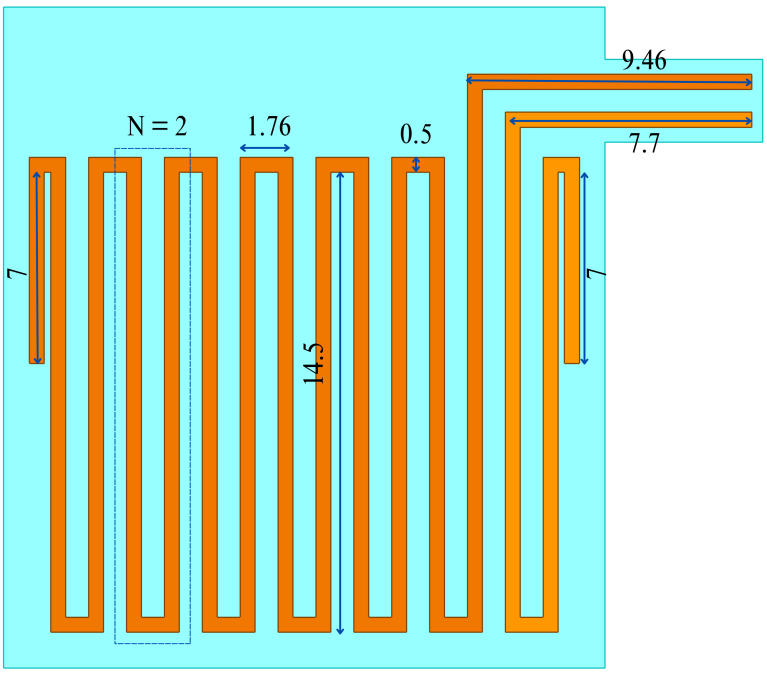

Figure 3.11. Optimized antenna (Unit: mm).

3.2. Eudragit as the Biodegradable Superstrate

In recent years, Eudragit has become a highly attractive area of research because of its significance in advanced drug delivery systems. Initially introduced by Rohm Haas GmbH, Darmstadt, in 1953, Eudragit serves as a drug coating that withstands acidic exposure while being soluble in alkaline environments. Today, it is marketed under the brand name Eudragit by Evonik Technologies Germany. Eudragit comprises a diverse range of neutral, cationic, and anionic copolymers derived from methacrylic acid and methacrylic or acrylic esters, as well as their derivatives. These copolymers are synthesized through various polymerization methods including reversible addition–fragmentation chain transfer (RAFT), atom transfer radical polymerization (ATRP), and group transfer polymerization. They have different levels of pH-dependent or independent solubility based on their physicochemical properties. Different types of Eudragit polymers are employed to selectively target various sections of the GI tract, including the small intestine, colon, and large intestine. Eudragit polymers are synthetic polyionic copolymers composed of varying concentrations of methacrylic acid esters, alkyl methacrylates, and 2-(dimethylamino)ethyl methacrylate. The specific properties and behavior of these copolymers are primarily determined by the concentrations of nonionized and ionized groups within their structure. Eudragit polymer grades are predominantly utilized for coating pharmaceutical formulations and developing advanced drug delivery systems [104].

Eudragit E100 is a positively charged copolymer made up of methyl methacrylate, dimethylaminoethyl methacrylate, and butyl methacrylate. Its chemical name is poly(butyl methacrylate-co-(2-dimethylaminoethyl) methacrylate-co-methyl methacrylate). It has an alkali value of 180 mg KOH/g, a molecular weight of approximately 47,000 g/mol, and shows low viscosity solubility at a gastric pH of 5.

Eudragit L100 is a negatively charged copolymer derived from methacrylic acid. It has a molecular weight of 125,000 g/mol, a glass transition temperature above 150°C, an acid value of 315 mg KOH/g, and is soluble at pH levels above 6.

Eudragit S100 is a negatively charged copolymer derived from methacrylic acid. It has a glass transition temperature above 150°C, an acid value of 190 mg KOH/g, a molecular weight of 125,000 g/mol, and is soluble in basic conditions at pH 7.0.

The pH sensitivity of the aforementioned Eudragit grades makes them ideal candidates for targeted drug delivery. Since different segments of the human GI tract exhibit varying pH levels, Eudragit polymers can effectively deliver drugs to specific regions of the digestive tract.The concept of targeted release inspired the idea of coating an ingestible capsule with three grades of Eudragit, each designed to dissolve at specific pH levels corresponding to the stomach, small intestine, and large intestine. This dissolution alters the near-field characteristics of the capsule's embedded antenna as it transitions through each organ. Finally, by monitoring the changes in the reflection coefficient of the antenna within each organ, we can identify the specific organ that contains the capsule [104].

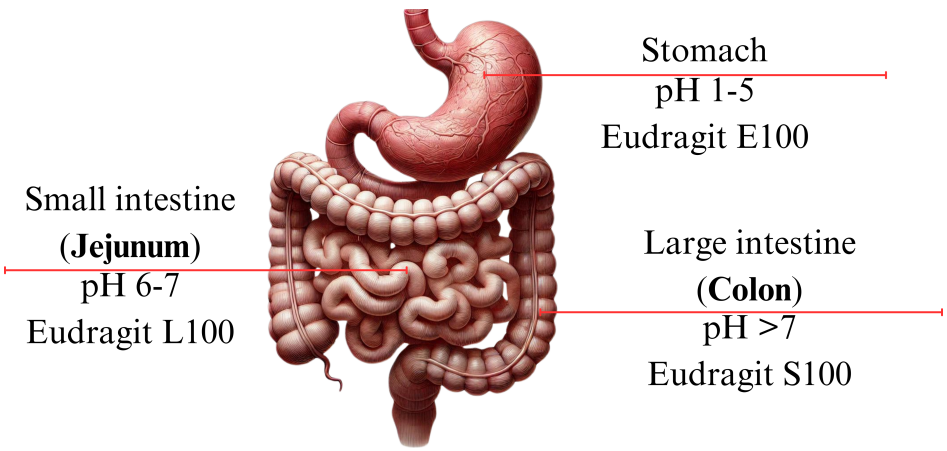

Figure 3.12. Eudragit grades for targeted drug delivery.

4. NUMERICAL RESULTS

Throughout this chapter, Ansys HFSS [105] simulations and their results are presented and explained. The section detailing the original ingestible capsule can be found in Section 4.1. Section 4.2 describes the operation of the optimized antenna embedded inside the coated capsule and explains how the degradation of the biodegradable superstrate while passing the stomach, small intestine, and large intestine affects the input response of the antenna. This biodegradation, which results in a shift in the center frequency of the antenna, forms the basis of our sensing mechanism.

4.1. Original Ingestible Capsule

The original capsule is depicted in Figures 4.1 and 4.2. Both offset-fed and coax-fed configurations are presented for comparative analysis.

The embedded antenna is designed to operate in the 433 MHz ISM band in a cylindrical homogeneous phantom (h = 120 mm, ⌀ = 100 mm). The phantom has the time-averaged electromagnetic properties of the GI tissues ($\varepsilon_r = 63$, $\sigma = 1.02$ S/m at 434 MHz, see [103]).

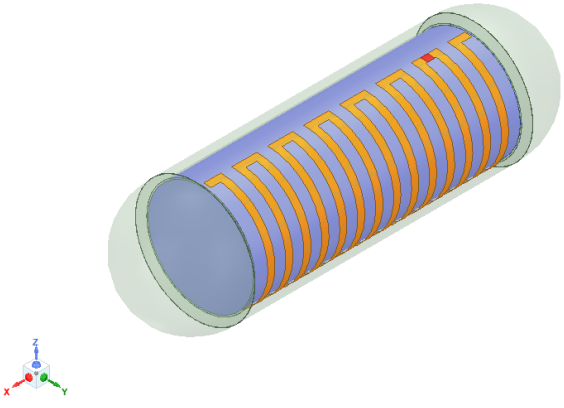

Figure 4.1. Offset-fed.

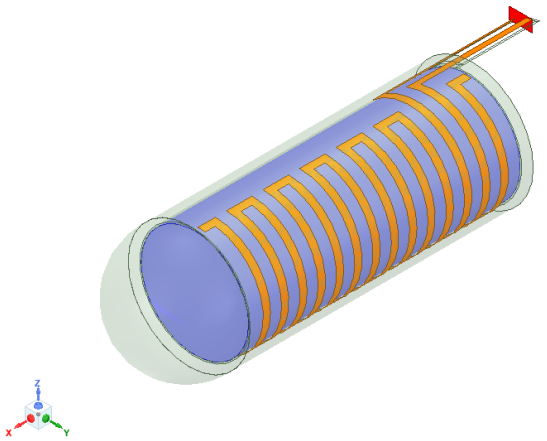

Figure 4.2. Coax-fed.

The magnitude and phase of the reflection coefficient of the embedded antenna can be seen in Figure 4.3 and Figure 4.4, respectively. The antenna operation in 434 MHz ISM band is shown.

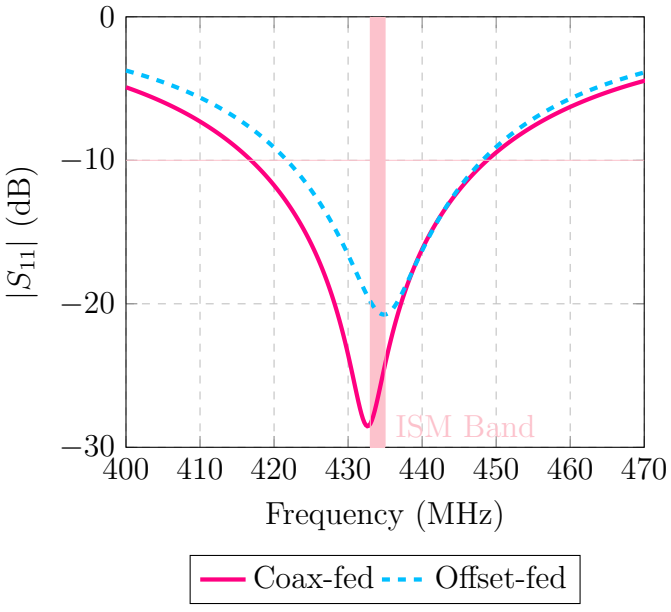

Figure 4.3. Simulated magnitude of the reflection coefficient of the original antenna.

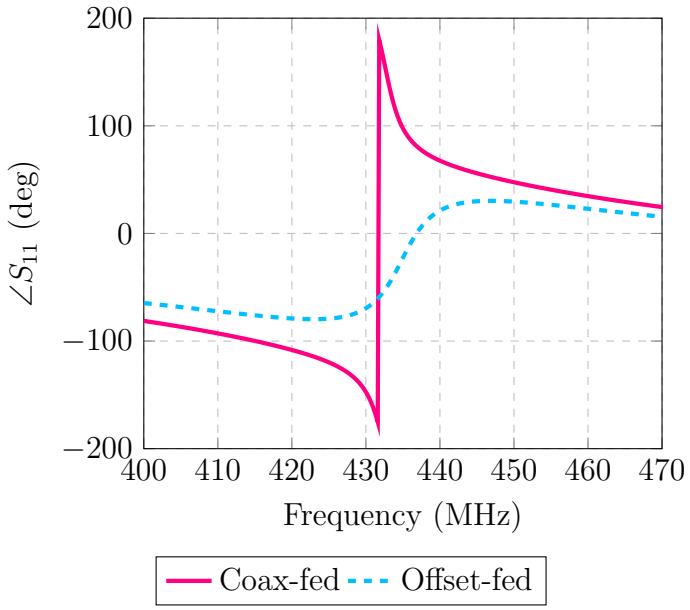

Figure 4.4. Simulated phase of the reflection coefficient of the original antenna.

However, addition of the 150 μm-thick ($\varepsilon_r = 5$, $\sigma = 1$ S/m) biodegradable superstrate results in detuning of the antenna as depicted in Figures 4.5 and 4.6. This clearly requires retuning of antenna parameters.

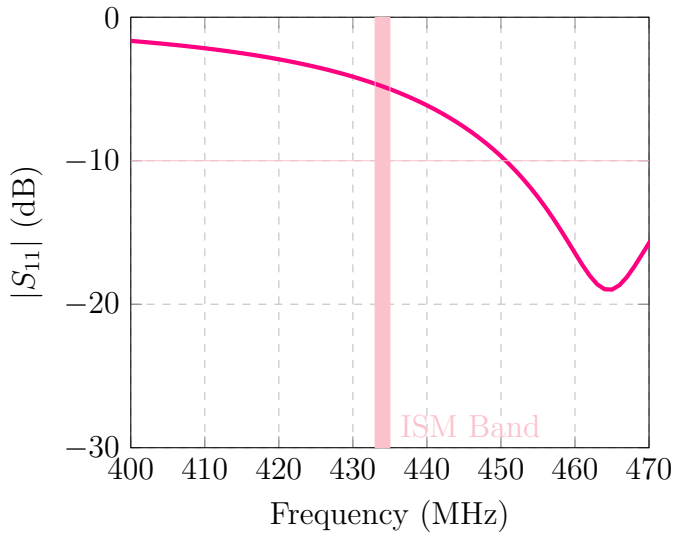

Figure 4.5. Simulated magnitude of the reflection coefficient of the original antenna after coating.

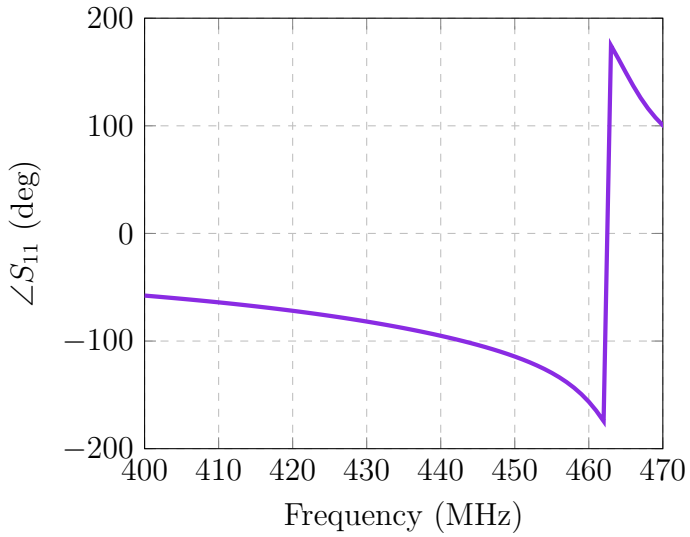

Figure 4.6. Simulated phase of the reflection coefficient of the original antenna after coating.

4.2. Tuning for desired operation

Coating the capsule decreases the effective permittivity, shifting the antenna's resonance frequency to a higher band by reducing the loading. To restore the antenna to the target 434 MHz ISM band, the dipole length was extended. This adjustment ensures continuous communication with the external reader throughout the GI tract, while the sensing coating undergoes biodegradation during transit. A detailed visualization of the optimized and coated capsule is provided in Figure 4.7.

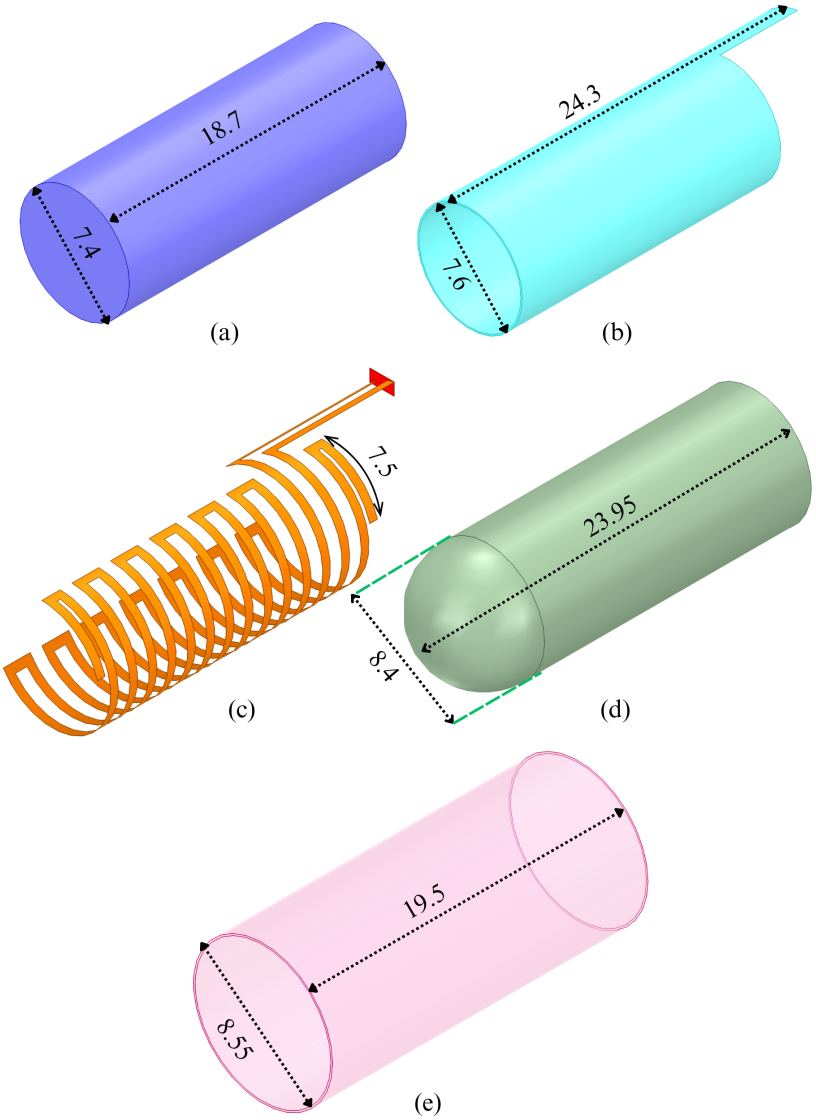

Figure 4.7. Capsule parts from the innermost to the outermost (unit: mm); a: air, b: Rogers CLTE-MW, c: Dipole, d: PLA, e: Biodegradable superstrate.

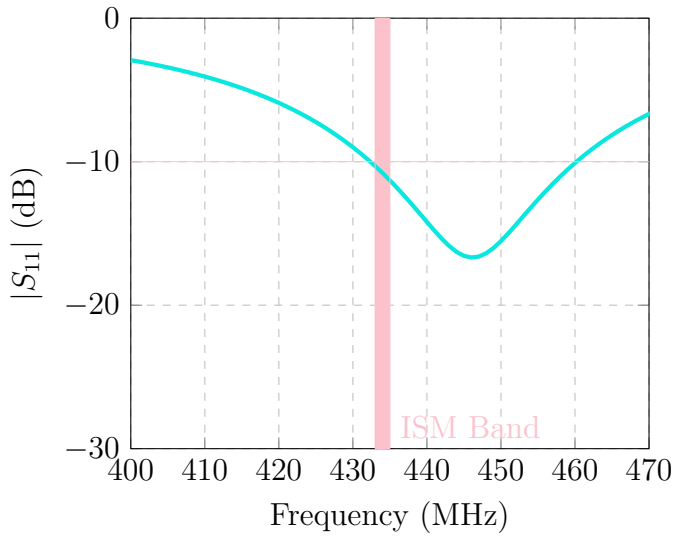

Figure 4.8. Simulated magnitude of the reflection coefficient of the optimized antenna with coated capsule.

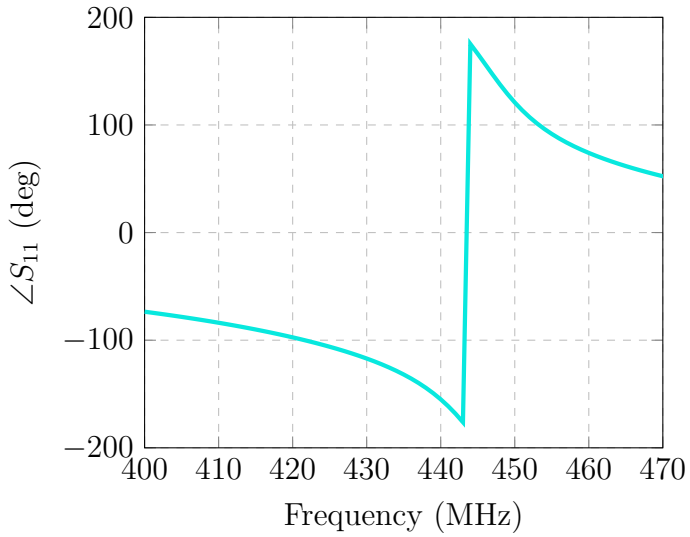

Figure 4.9. Simulated phase of the reflection coefficient of the optimized antenna with coated capsule.

The frequency-dependent dielectric properties of the stomach, small intestine, and large intestine are presented next. The subsequent three steps of our simulations involve solving for the input response of the antenna in these three environments, taking into account the biodegradation of the designated region.

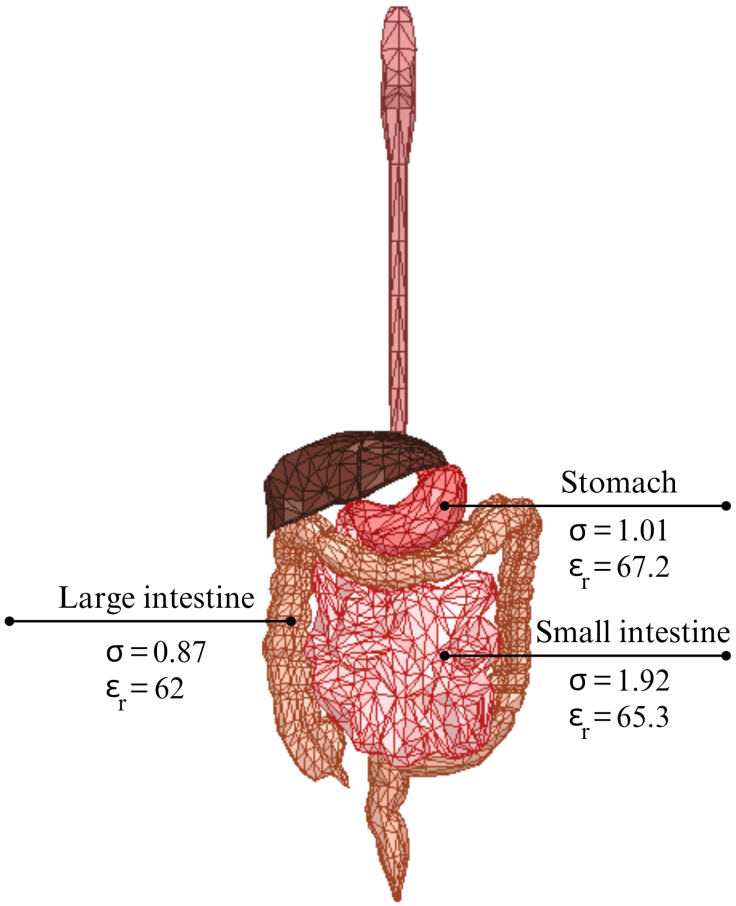

Figure 4.10. Dielectric properties of human GI tract at = 433 MHz, (σ is in S/m unit).

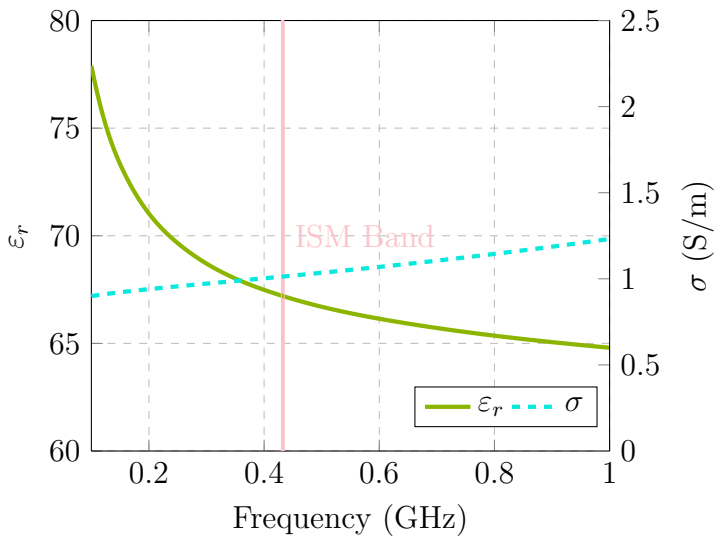

Figure 4.11. Frequency-dependent dielectric properties of human stomach [106].

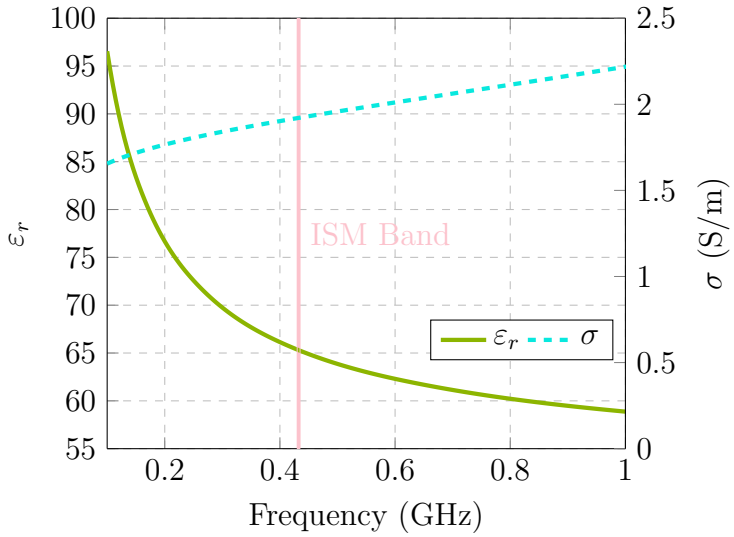

Figure 4.12. Frequency-dependent dielectric properties of human small intestine [106].

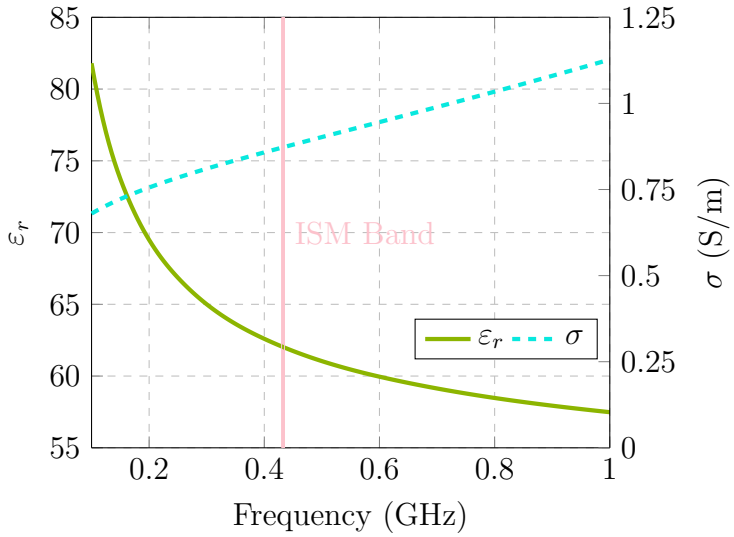

Figure 4.13. Frequency-dependent dielectric properties of human large intestine [106].

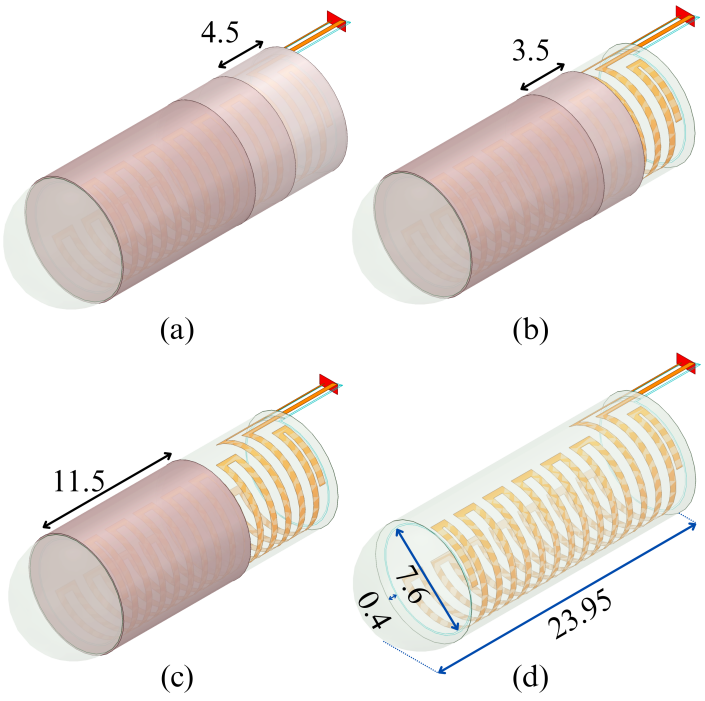

Figure 4.14. Capsule model and three consecutive degradation steps (unit: mm); a: Initial, b: Stomach, c: Small intestine, d: Large intestine.

Figure 4.15 and 4.16 show the simulated magnitude and phase response of the antenna, respectively, in the initial state and in three GI tissues. The center frequency of the antenna for each case and the magnitude and the phase of the reflection at these center frequencies are tabulated in Table 4.1. Furthermore, the magnitude and the phase values at 434 MHz for all cases are tabulated in Table 4.2. As can be seen from Table 4.1, a shift of at least 5 MHz in the center frequency of the antenna is observed at each degradation step. A similar trend is visible in the phase of the reflection coefficient. Finally, the magnitude and phase at 434 MHz change notably at each step allowing for segment tracking. Note that at each step, the antenna is operational for the whole band. This demonstrates that the proposed technique does not intercept the normal operation of the capsule.

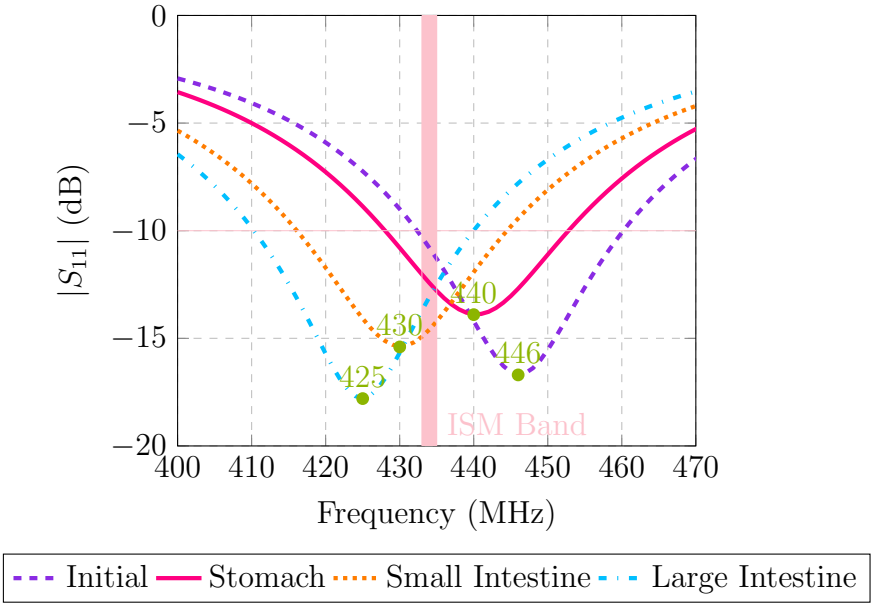

Figure 4.15. Simulated magnitude of the reflection coefficient for different degradation steps.

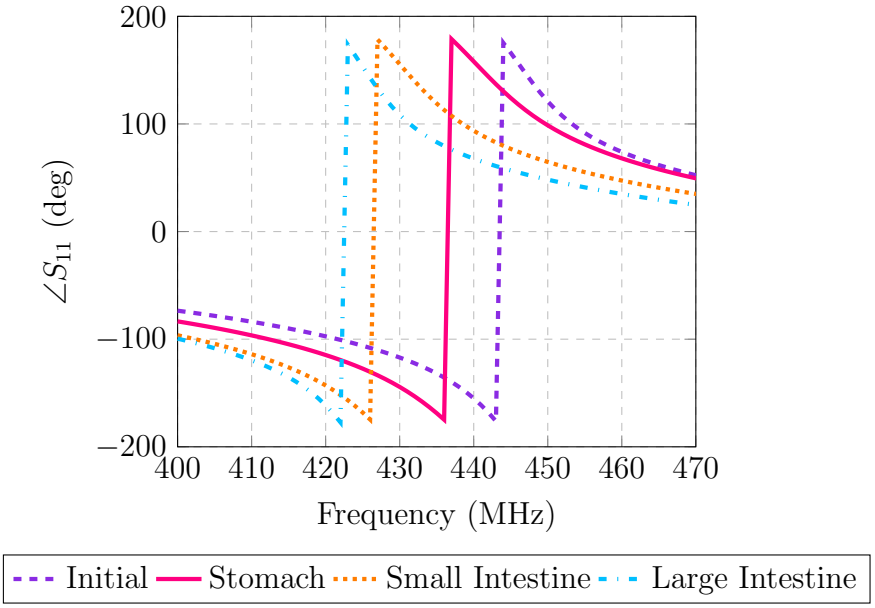

Figure 4.16. Simulated phase of the reflection coefficient for different degradation steps.

Table 4.1. Center frequency of the antenna for different degradation steps and magnitude and phase of the reflection coefficient at corresponding center frequencies.

Degradation Step	f_c (MHz)	$\lvert S_{11}\rvert$ (dB)	$\angle S_{11}$ (deg)
Initial	446	-16.7	156.5
Stomach	440	-13.9	158
Small Intestine	430	-15.4	155.5
Large Intestine	425	-17.8	153

Table 4.2. Simulated magnitude and phase of the reflection coefficient at 434 MHz for the different degradation steps.

Degradation Step	$\lvert S_{11}\rvert$ (dB)	$\angle S_{11}$ (deg)
Initial	-10.8	-128.4
Stomach	-12.4	-163
Small Intestine	-14.6	125.5
Large Intestine	-13.1	87.1

5. MEASUREMENTS

The experimental results will be presented and discussed in this chapter. The experimental setup is introduced in Section 5.1. Subsequently, the capsule coating is explained in Section 5.2. Next, the liquid electrochemical phantoms mimicking the GI tract organs are presented in Section 5.3. Section 5.4 explains the experimental procedures and provides the measurement results. Finally, Section 5.5 discusses the observations from the experiments.

5.1. Measurement Setup

Figure 5.10 shows the experimental setup used in our work.

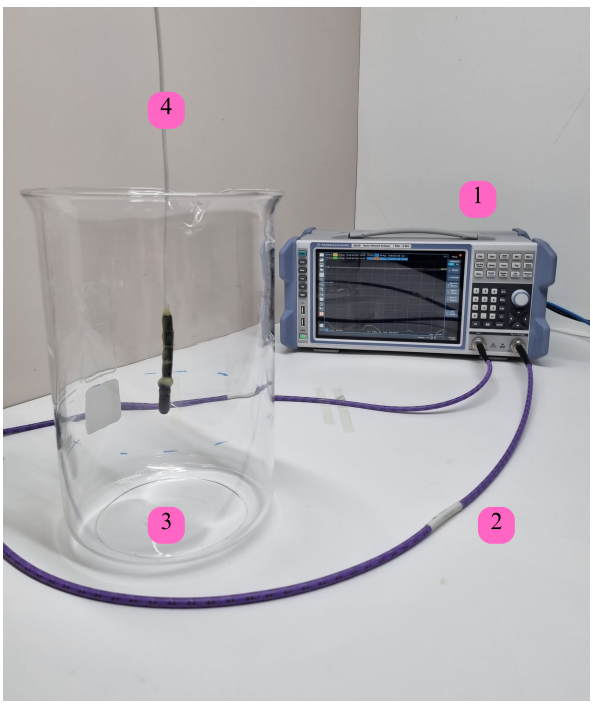

Figure 5.1. 1: RHODE & SCHWARZ ZNLE6 Vector Network Analyzer, 2: Qualwave QT50P-18-3N-1 Test Cable Assembly, 3: ISOLAB 025.01.905 Glass Beaker, 4: Capsule Under Test

5.2. Capsule Coating

The capsule was coated using polymer solutions prepared with a solvent mixture of 60% acetone and 40% isopropyl alcohol. Specifically, S 100 and L 100 polymers were prepared at a concentration of 25 wt.%, while E 100 was prepared at 50 wt.%. To protect areas not intended for coating, the ends of the capsule were covered with parafilm, and a 2.5 mm section of the capsule was masked with label paper as seen in Figure 5.2(b) and Figure 5.2(c). The S 100 polymer was then applied using a dip coating device at a speed of 150 mm/min, with manual control over the process, See Figures 5.2(d) - Figure 5.2(h). After the coating dried as in Figure 5.2(i), a snap blade knife was used to cut the coating at the mask level, making it easier to remove the mask.

Next, a 2 mm section of the capsule was re-masked as shown in Figure 5.2(j) and Figure 5.2(k), covering the previously coated S 100 section, and the L 100 polymer was applied as in Figure 5.2(l). Once the dip-coated L 100 had dried as can be seen in Figure 5.2(m), the coating was cut again with a snap blade knife to facilitate removal. Finally, the sections coated with S 100 and L 100 were covered, and a final coating of E 100 was applied to the capsule, see Figure 5.2(n) - Figure 5.2(r) for this.

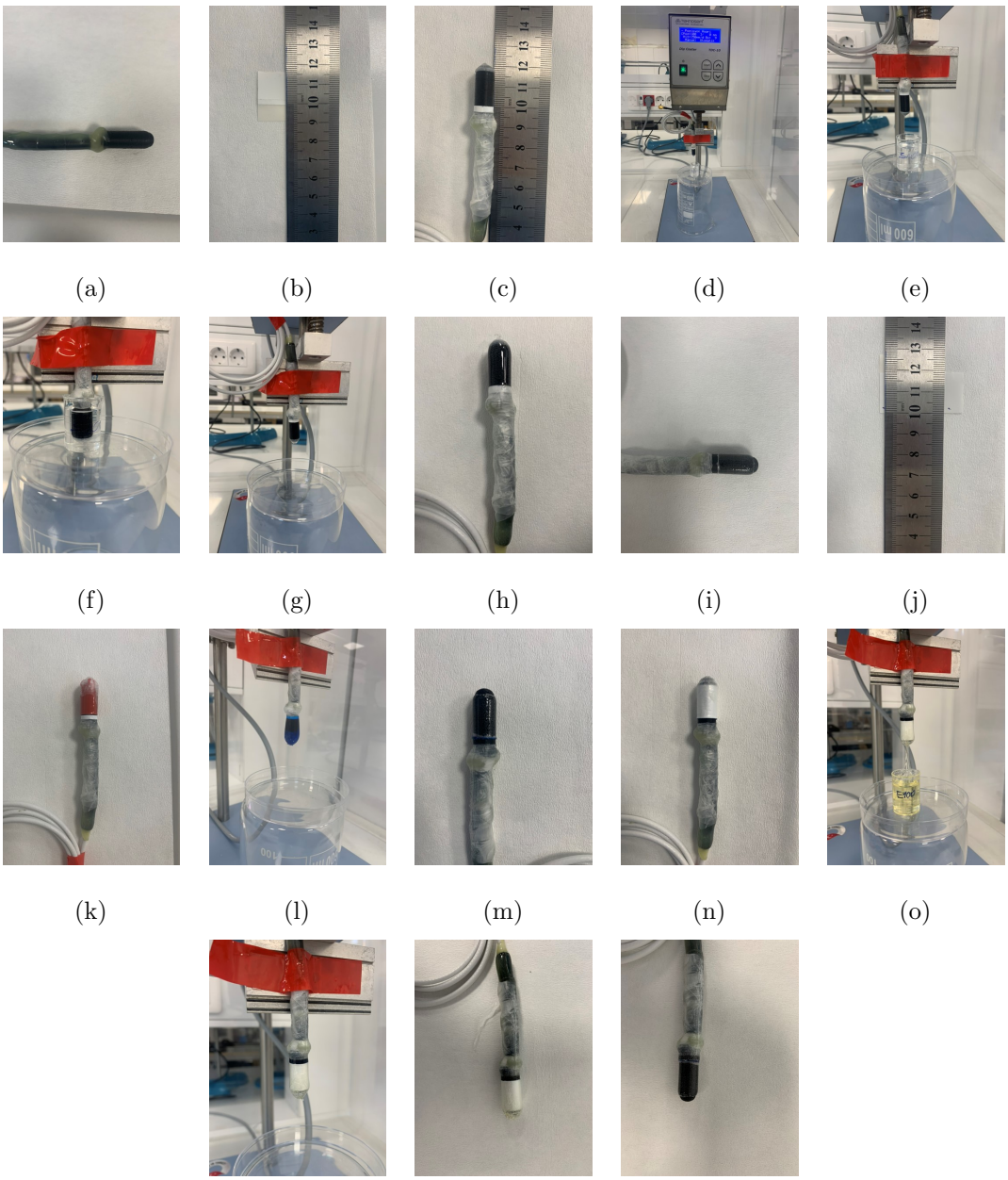

Figure 5.2. Coating procedure; a: Bare capsule, b-i: S 100 coating, j-m: L 100 coating, n-r: E 100 coating.

5.3. Phantom Production

Electrochemical phantoms replicating the dielectric properties at 434 MHz and pH of the human stomach, small intestine, and large intestine were developed under ambient temperatures of 20°C - 21°C.

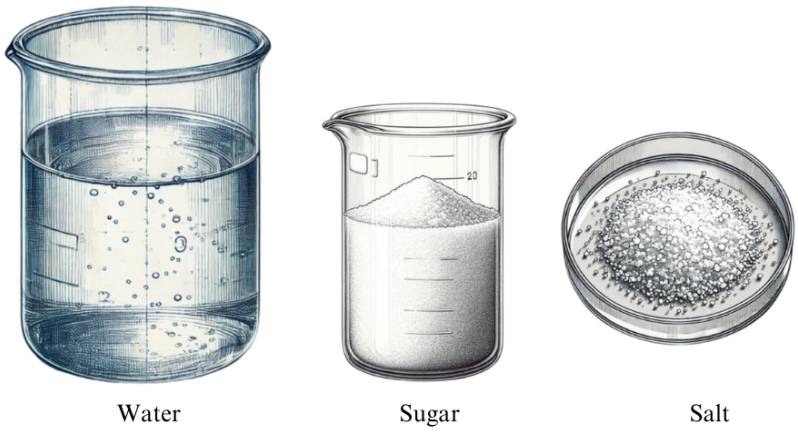

Figure 5.3. Phantom content

After mixing the necessary amounts of each component, the mixture will be stirred on the hot plate long enough to achieve a clear phantom. Table 5.1 shows the concentrations for each phantom and each phantom's dielectric properties. These dielectric properties were measured using SPEAG DAK-3.5, as shown in Figure 5.4.

Figure 5.4. SPEAG DAK-3.5.

Table 5.1. Electrochemical properties and concentrations (in grams) per 100 grams for the fabrication of phantoms mimicking the EM characteristics of the GI tract.

GI Segment	Water	Salt	Sugar	ε_r	σ	pH
Stomach	68.5	1.1	30.4	67.42	1.01	6.8
Small Intestine	67	2.5	30.5	65.38	2	6.8
Large Intestine	71	1.5	27.5	62.4	0.89	6.8

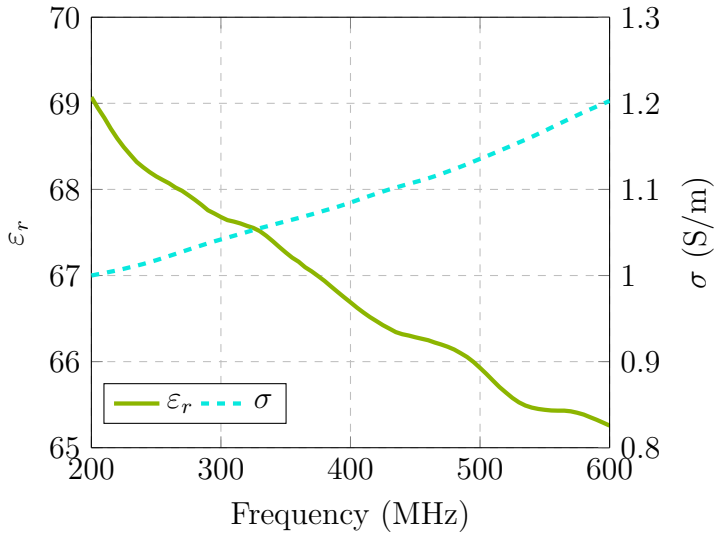

Figure 5.5. Frequency-dependent dielectric properties of human stomach phantom.

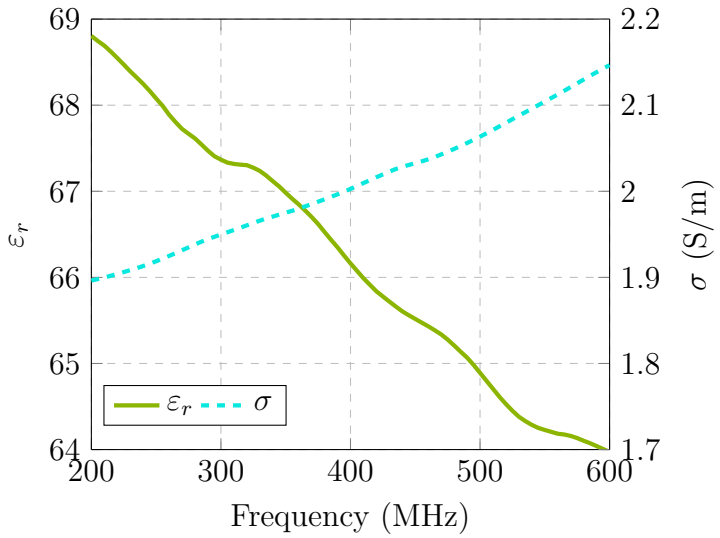

Figure 5.6. Frequency-dependent dielectric properties of human small intestine phantom.

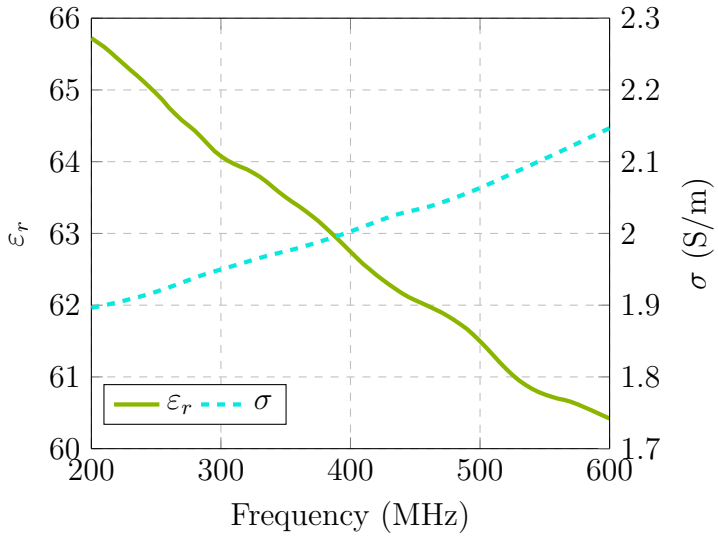

Figure 5.7. Frequency-dependent dielectric properties of human large intestine phantom.

After validating the electromagnetic properties, chemical mimicking was performed using citric acid and sodium hydroxide to adjust the pH to the desired levels. Table 5.2 summarizes the required quantities for achieving the target pH values and presents the corresponding electromagnetic properties after pH adjustment. Notably, pH mimicking had no impact on the EM properties of the phantoms.

Table 5.2. pH and concentrations (in milligrams) per 1000 grams for the fabrication of phantoms mimicking the EM properties of the GI tract.

GI Segment	Citric Acid	Sodium Hydroxide	pH	ε_r	σ
Stomach	1200	0	3	67.42	1.01
Small Intestine	0	0	6.8	65.38	2
Large Intestine	0	1	8.4	62.4	0.89

Finally, for every 1000 grams of phantom, 0.3 grams of sodium azide was added to inhibit bacterial growth.

Table 5.3. Dielectric properties of stomach, small intestine and large intestine phantoms at 434 MHz, reference values provided by [106] for these tissues are also given for comparative purposes.

	ε_r	σ [S/m]
Stomach phantom	66.3	1.1
Measured stomach	67.2	1.01
Small intestine phantom	65.66	2.02
measured small intestine	65.3	1.92
Large intestine phantom	62.22	0.93
measured large intestine	62	0.87

5.4. Measurements and Results

Our ingestible capsule was coated with three grades of Eudragit polymer, as depicted in Figure 5.10. The coating length for each grade was determined based on numerical simulations. Figures 5.8 and 5.9 illustrate the magnitude and phase of the reflection coefficient of the embedded antenna, respectively. As shown in the plots, the capsule-embedded antenna is detuned and now operates at 344 MHz. Two key points should be noted: first, the fabrication of the ingestible capsule was performed by our collaborators and falls outside the scope of this work. Second, the antenna detuning does not compromise the validity of our method, as the proof of concept remains independent of the antenna type or operating frequency.

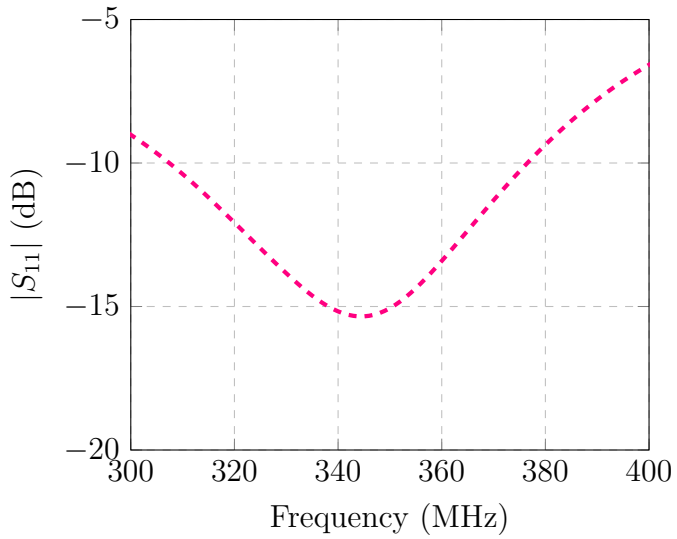

Figure 5.8. Measured magnitude of the reflection coefficient of the capsule embedded antenna.

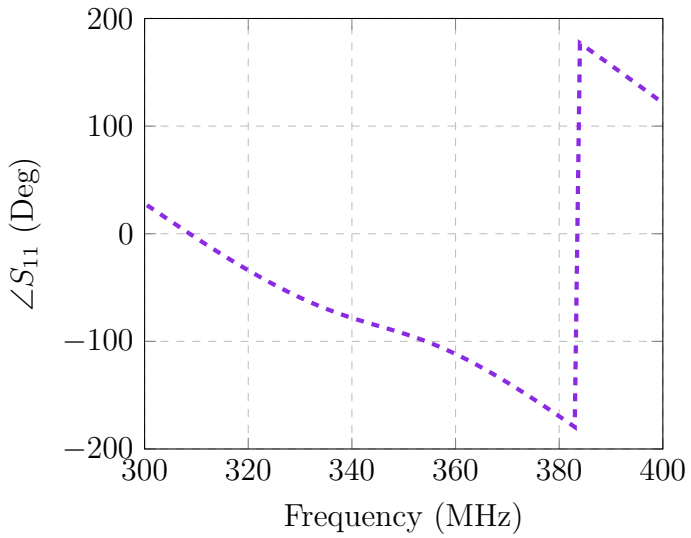

Figure 5.9. Measured phase of the reflection coefficient of the capsule embedded antenna.

Our prepared phantoms accurately mimic the electromagnetic properties at 344 MHz, and thus, we continued using the same phantoms. Table 5.4 presents the EM properties of these phantoms at 344 MHz.

Table 5.4. Dielectric properties of stomach, small intestine and large intestine phantoms at 344 MHz, values provided by [106] for these tissues are also given for comparative purposes.

	ε_r	σ [S/m]
Stomach phantom	67.3	1.06
Measured stomach	68.1	0.98
Small intestine phantom	67.05	1.97
measured small intestine	67.9	1.87
Large intestine phantom	63.57	0.87
measured large intestine	63.8	0.83

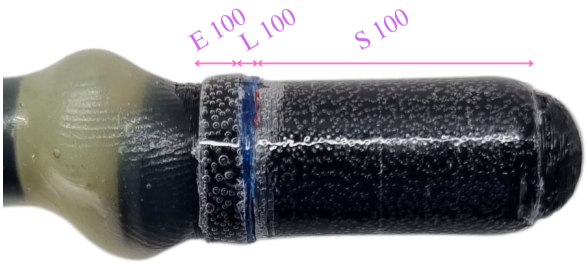

Figure 5.10. Coated capsule.

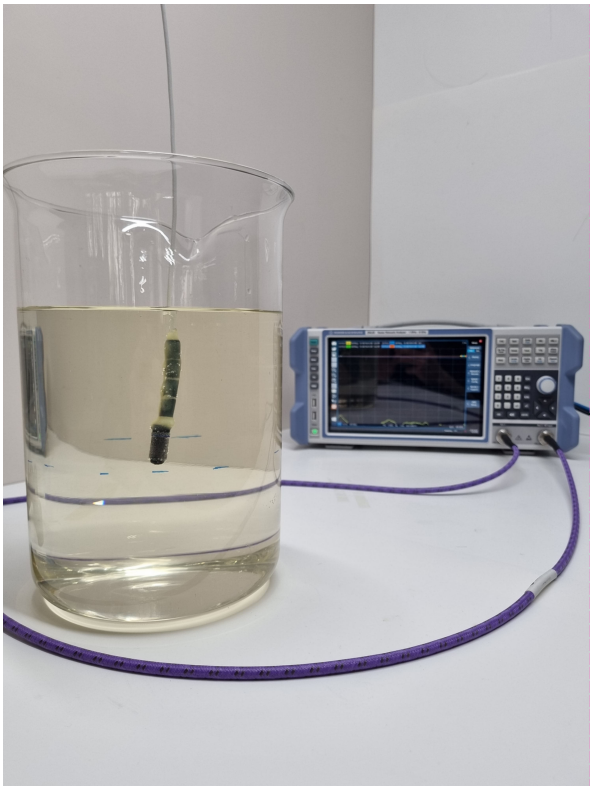

Figure 5.11. In stomach.

Figure 5.12. Leaving stomach.

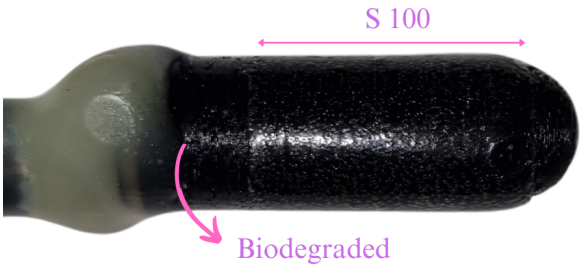

Figure 5.13. Leaving small intestine.

Figure 5.14. Leaving large intestine.

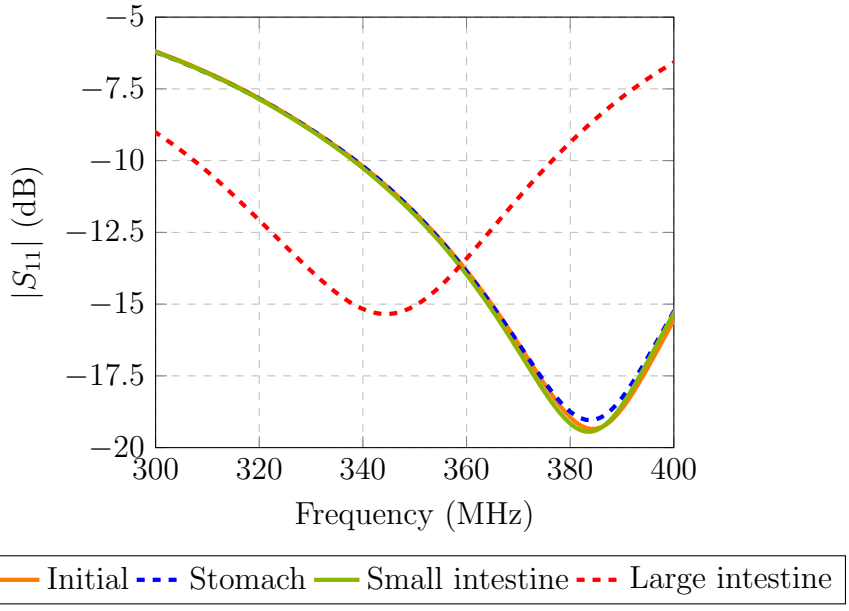

Figure 5.15. Measured magnitude of the reflection coefficient of the capsule embedded antenna for different degradation steps.

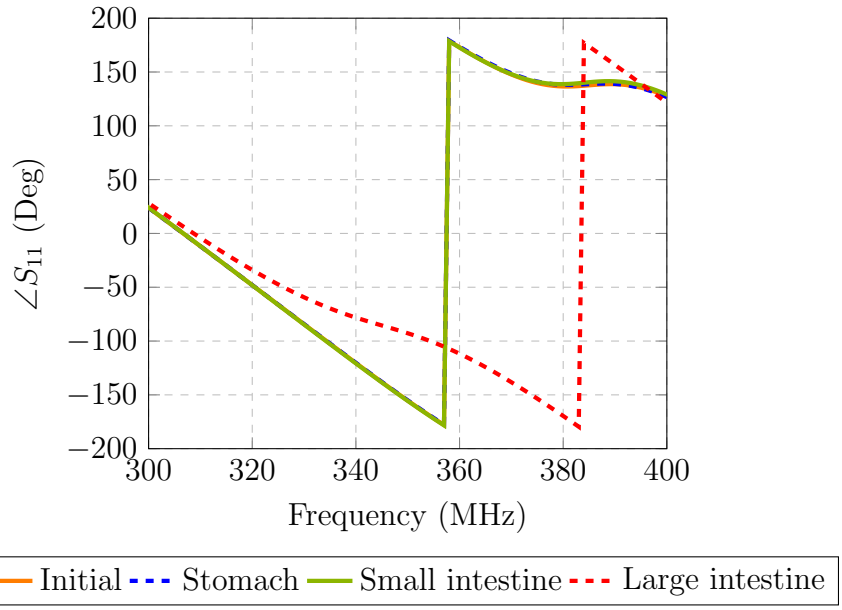

Figure 5.16. Measured phase of the reflection coefficient of the capsule-embedded antenna for different degradation steps.

Table 5.5. Measured center frequency of the antenna for different degradation steps and reflection coefficient plots at corresponding center frequencies.

Degradation Step	f_c (MHz)	$\lvert S_{11}\rvert$ (dB)	$\angle S_{11}$ (deg)
Initial	384	-19.3	137.2
Stomach	384	-19	138.5
Small Intestine	384	-19.4	140
Large Intestine	344	-15.3	-84

5.5. Discussion

As discussed in Chapter 4, simulations clearly demonstrated the capsule's transition from the stomach to the small intestine, and subsequently to the large intestine. However, these simulations were conducted using an approximate dielectric constant, and our coating thicknesses were not precisely controlled. These approximations were expected to cause discrepancies between our measurements and the simulations. As shown, we were only able to detect the capsule's location in the large intestine.

We anticipate that precise measurements of the dielectric constant of Eudragit grades and better control over coating thickness would enhance the correlation between measurements and simulations. However, at this stage, we lacked access to the required infrastructure, such as the SPEAG DAK-TL2, which is used for measuring thin films.

6. CONCLUSION

Gastrointestinal tract health is a critical factor in an individual's overall well-being, making its monitoring highly valuable. Ingestible capsules can collect and transmit data from various regions of the digestive tract, providing access to areas that were previously difficult to reach. However, these valuable tools still lack a crucial element that impacts the validity of interpretation of the received data: location information.

This work introduces a technique that leverages the intrinsic electrochemical characteristics of the stomach, small intestine, and large intestine to determine the location of an ingestible capsule. Eudragit, a commercially available family of polymers used for targeted drug delivery, is employed in this method. Three grades of Eudragit—E 100, L 100, and S 100—are coated around the capsule to form three superstrate regions, each soluble only in one of the three targeted organs. Simulations on a 150 µm superstrate with approximate electromagnetic values were conducted.

Once the capsule is ingested, it remains intact in terms of its coating until it reaches the acidic environment of the stomach. Here, E 100 dissolves, causing the ingestible antenna embedded within the capsule to lose one superstrate region and shift its resonance frequency. This transition from an initial intact state to a shifted center frequency is shown to be 6 MHz. The same scenario applies for L 100 when the capsule travels from the stomach to the small intestine, and for S 100 when it moves from the small intestine to the large intestine. The frequency shift for the second transition is 10 MHz, and the last transition results in a 5 MHz resonance shift. This variation in center frequency indicates the capsule's location.

Based on the simulations, electromagnetic measurements were conducted to observe the variations in electrochemical phantoms that mimic both the dielectric properties and pH of each of the three organs. The resonance shift is observed to be 40

MHz when the capsule moves from the small intestine to the large intestine. However, due to uncontrolled coating thickness and approximate dielectric properties, we were unable to observe a variation in resonance in the first two location transitions.

The novelty of this method lies primarily in its integrability with any ingestible capsule. To the author's best knowledge, this is the first instance of pH sensing along the GI tract using a biodegradable sensor introduced in the literature.

In the future, we plan to obtain the exact dielectric properties of the Eudragit grades and perform more controlled coatings to better align our simulations with the measurements.

7. FUTURE WORK

By employing more advanced coating techniques, we plan to further advance our application. Our goal is to develop the addition of a passive resonator and control its biodegradation using pH-dependent polymers, thereby bringing this concept into practical implementation.

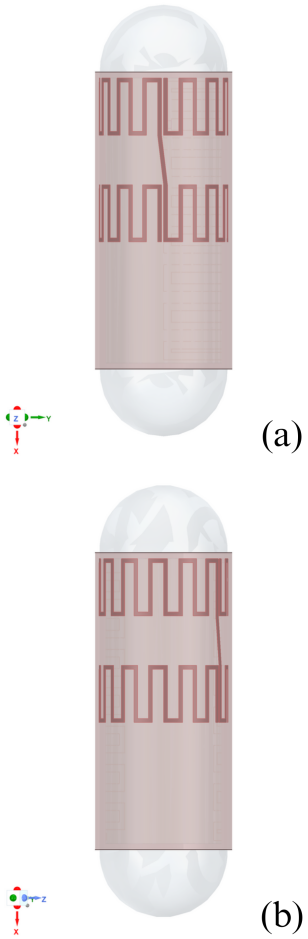

Figure 7.1. Coated capsule with resonator from two different views; a: Top view, b: Custom view ($\Psi = 90$, $\theta = 30$, $\phi = -90$).

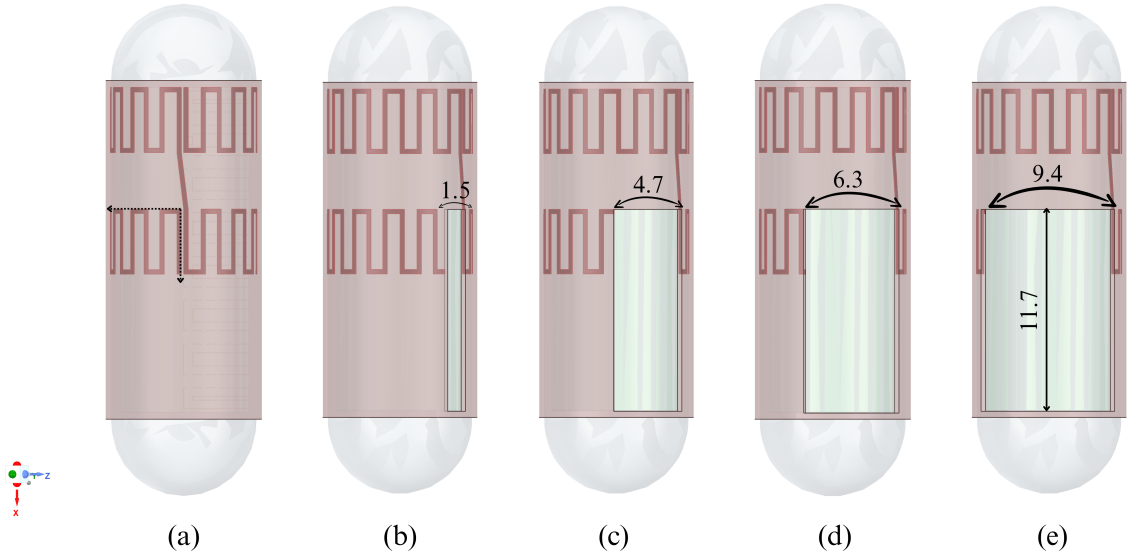

Figure 7.2. Degradation flow (unit: mm); a: The origin and direction of degradation, b-e: degradation steps.

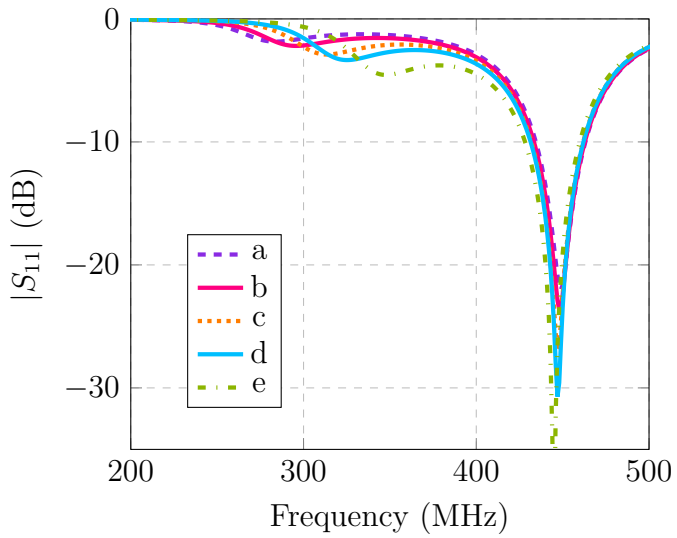

Figure 7.3. Simulated magnitude of the reflection coefficient for different degradation steps.

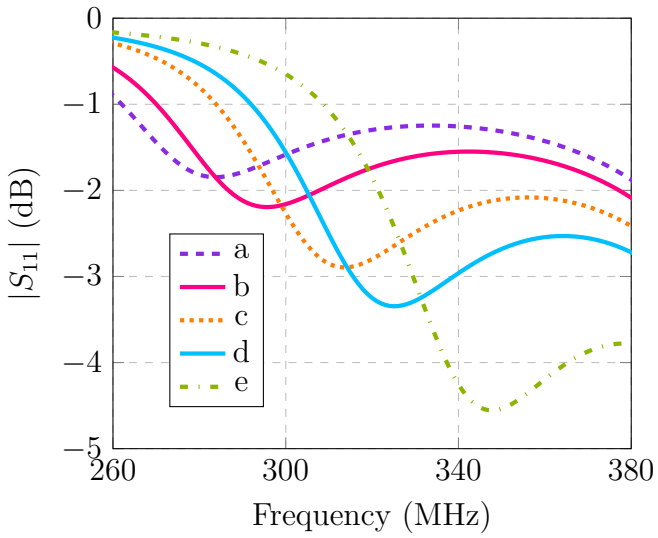

Figure 7.4. Simulated magnitude of the reflection coefficient for different degradation steps; magnified for better observation.

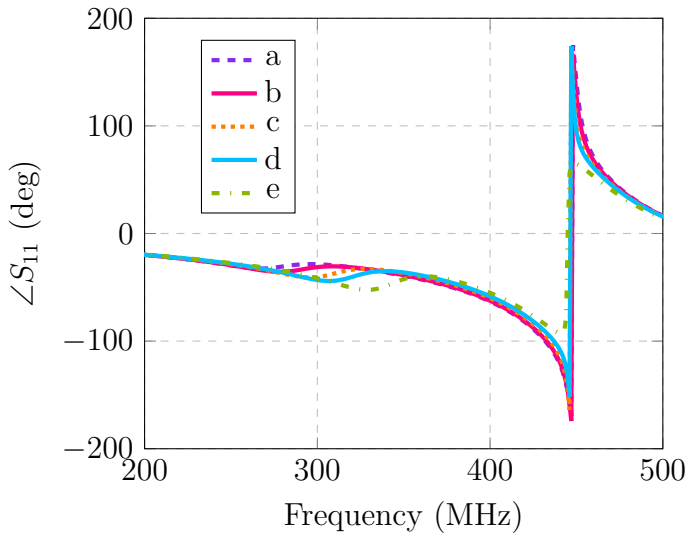

Figure 7.5. Simulated phase of the reflection coefficient for different degradation steps.

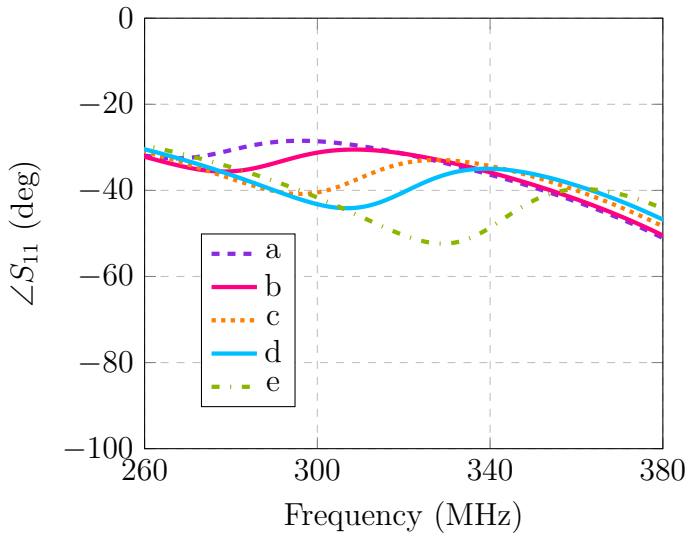

Figure 7.6. Simulated phase of the reflection coefficient for different degradation steps; magnified for better observation.

REFERENCES

1. Zimmerman, T. G., *Personal Area Networks (PAN): Near-Field Intra-Body Communication*, Master's Thesis, Massachusetts Institute of Technology, 1995.

2. IEEE 802.15 Working Group, "Task Group 6 (TG6): Body Area Networks", `https://www.ieee802.org/15/pub/TG6.html`, 2011, accessed on July 08, 2024.

3. Latré, B., B. Braem, I. Moerman, C. Blondia and P. Demeester, "A Survey on Wireless Body Area Networks", *Wireless Networks*, Vol. 17, pp. 1–18, 2011.

4. Xia, F., Y.-C. Tian, Y. Li and Y. Sun, "Wireless Sensor/Actuator Network Design for Mobile Control Applications", *Sensors*, Vol. 7, No. 10, pp. 2157–2173, 2007.

5. Movassaghi, S., M. Abolhasan, J. Lipman, D. Smith and A. Jamalipour, "Wireless Body Area Networks: A Survey", *IEEE Communications Surveys & Tutorials*, Vol. 16, No. 3, pp. 1658–1686, 2014.

6. Kwak, K. S., S. Ullah and N. Ullah, "An Overview of IEEE 802.15.6 Standard", *Proceedings of the 2010 3rd International Symposium on Applied Sciences in Biomedical and Communication Technologies (ISABEL)*, pp. 1–6, Rome, Italy, 2010.

7. Otto, C., A. Milenković, C. Sanders and E. Jovanov, "System Architecture of a Wireless Body Area Sensor Network for Ubiquitous Health Monitoring", *Journal of Mobile Multimedia*, Vol. 1, No. 4, pp. 307–326, 2006.

8. Dishman, E., "Inventing Wellness Systems for Aging in Place", *Computer*, Vol. 37, No. 5, pp. 34–41, 2004.

9. Khan, A. N., Y.-O. Cha, H. Giddens and Y. Hao, "Recent Advances in Organ Specific Wireless Bioelectronic Devices: Perspective on Biotelemetry and Power

Transfer Using Antenna Systems", *Engineering*, Vol. 11, pp. 27–41, 2022.

10. Steiger, C., A. Abramson, P. Nadeau, A. P. Chandrakasan, R. Langer and G. Traverso, "Ingestible Electronics for Diagnostics and Therapy", *Nature Reviews Materials*, Vol. 4, pp. 83–98, 2019.

11. Miller, L., A. Farajidavar and A. Vegesna, "Use of Bioelectronics in the Gastrointestinal Tract", *Cold Spring Harbor Perspectives in Medicine*, Vol. 9, No. 9, p. a034165, 2019.

12. Keller, J., G. Bassotti, J. Clarke, P. Dinning, M. Fox, M. Grover, P. M. Hellström, M. Ke, P. Layer, C. Malagelada, H. P. Parkman, S. M. Scott, J. Tack, M. Simren, H. Törnblom and M. Camilleri, "Advances in the Diagnosis and Classification of Gastric and Intestinal Motility Disorders", *Nature Reviews Gastroenterology & Hepatology*, Vol. 15, No. 5, pp. 291–308, 2018.

13. Rao, S. S. C., M. Camilleri, W. L. Hasler, A. H. Maurer, H. P. Parkman, R. Saad, M. S. Scott, M. Simren, E. Soffer, and L. Szarka, "Evaluation of Gastrointestinal Transit in Clinical Practice: Position Paper of the American and European Neurogastroenterology and Motility Societies", *Neurogastroenterology & Motility*, Vol. 23, No. 1, pp. 8–23, 2011.

14. Mimee, M., P. Nadeau, A. Hayward, S. Carim, S. Flanagan, L. Jerger, J. Collins, S. McDonnell, R. Swartwout, R. J. Citorik, V. Bulović, R. Langer, G. Traverso, A. P. Chandrakasan and T. K. Lu, "An Ingestible Bacterial-Electronic System to Monitor Gastrointestinal Health", *Science*, Vol. 360, No. 6391, pp. 915–918, 2018.

15. Kuo, B., R. W. McCallum, K. L. Koch, M. D. Sitrin, J. M. Wo, W. D. Chey, W. L. Hasler, J. M. Lackner, L. A. Katz, J. R. Semler, G. E. Wilding and H. P. Parkman, "Comparison of Gastric Emptying of a Nondigestible Capsule to a Radio-Labelled Meal in Healthy and Gastroparetic Subjects", *Alimentary Phar-*

macology & Therapeutics, Vol. 27, No. 2, pp. 186–196, 2008.

16. Kobayashi, Y., A. Yamada, H. Watabe, R. Takahashi, H. Suzuki, Y. Hirata, Y. Yamaji, H. Yoshida and K. Koike, "Sonographic Detection of a Patency Capsule Prior to Capsule Endoscopy: Case Report", *Journal of Clinical Ultrasound*, Vol. 42, No. 9, pp. 554–556, 2014.

17. Sharma, S., K. B. Ramadi, N. H. Poole, S. S. Srinivasan, K. Ishida, J. Kuosmanen, J. Jenkins, F. Aghlmand, M. B. Swift, M. G. Shapiro, G. Traverso and A. Emami, "Location-Aware Ingestible Microdevices for Wireless Monitoring of Gastrointestinal Dynamics", *Nature Electronics*, Vol. 6, No. 3, pp. 242–256, 2023.

18. Wang, A., S. Banerjee, B. A. Barth, Y. M. Bhat, S. Chauhan, K. T. Gottlieb, V. Konda, J. T. Maple, F. Murad, P. R. Pfau, D. K. Pleskow, U. D. Siddiqui, J. L. Tokar, S. A. Rodriguez and A. T. Committee, "Wireless Capsule Endoscopy", *Gastrointestinal Endoscopy*, Vol. 78, No. 6, pp. 805–815, 2013.

19. Hejazi, R. A., M. Bashashati, M. Saadi, Z. D. Mulla, I. Sarosiek, R. W. McCallum and M. J. Zuckerman, "Video Capsule Endoscopy: A Tool for the Assessment of Small Bowel Transit Time", *Frontiers in Medicine*, Vol. 3, p. 6, 2016.

20. Maqbool, S., H. P. Parkman and F. K. Friedenberg, "Wireless Capsule Motility: Comparison of the SmartPill GI Monitoring System with Scintigraphy for Measuring Whole Gut Transit", *Digestive Diseases and Sciences*, Vol. 54, No. 10, pp. 2167–2174, 2009.

21. Dagdeviren, C., F. Javida, P. Joe, T. von Erlach, T. Bensel, Z. Wei, S. Saxton, C. Cleveland, L. Booth, S. McDonnell, J. Collins, A. Hayward, R. Langer and G. Traverso, "Flexible Piezoelectric Devices for Gastrointestinal Motility Sensing", *Nature Biomedical Engineering*, Vol. 1, No. 10, pp. 807–817, 2017.

22. Haase, A.-M., S. Fallet, M. Otto, S. M. Scott, V. Schlageter and K. Krogh, "Gas-

trointestinal Motility During Sleep Assessed by Tracking of Telemetric Capsules Combined With Polysomnography – A Pilot Study", *Clinical and Experimental Gastroenterology*, Vol. 8, pp. 327–332, 2015.

23. Gharibans, A. A., B. L. Smarr, D. C. Kunkel, L. J. Kriegsfeld, H. M. Mousa and T. P. Coleman, "Artifact Rejection Methodology Enables Continuous, Non-invasive Measurement of Gastric Myoelectric Activity in Ambulatory Subjects", *Scientific Reports*, Vol. 8, p. 5019, 2018.

24. Mateen, H., M. R. Basar, A. U. Ahmed and M. Y. Ahmad, "Localization of Wireless Capsule Endoscope: A Systematic Review", *IEEE Sensors Journal*, Vol. 17, No. 5, pp. 1197–1206, 2017.

25. Ladić, K., *Enabling Communication and Localization Technologies for Wireless Capsule Endoscopy*, Ph.D. Thesis, University of Zagreb, Faculty of Electrical Engineering and Computing, 2024.

26. Bianchi, F., A. Masaracchia, E. S. Barjuei, A. Menciassi, A. Arezzo, A. Koulaouzidis, D. Stoyanov, P. Dario and G. Ciuti, "Localization Strategies for Robotic Endoscopic Capsules: A Review", *Expert Review of Medical Devices*, Vol. 16, No. 5, pp. 381–403, 2019.

27. Yao, L., S. R. Khan, G. Dolmans, J. Romme and S. Mitra, "High Accuracy Localization for Miniature Ingestible Devices Using Mutual Inductance", *IEEE Transactions on Biomedical Circuits and Systems*, Vol. 18, No. 3, pp. 662–678, 2024.

28. Zeising, S., A. S. Thalmayer, M. Lübke, G. Fischer and J. Kirchner, "Localization of Passively Guided Capsule Endoscopes—A Review", *IEEE Sensors Journal*, Vol. 22, No. 21, pp. 20138–20155, 2022.

29. Bjørnevik, A. S., *Localization and Tracking of Intestinal Paths for Wireless Cap-*

sule Endoscopy, Master's Thesis, Norwegian University of Science and Technology, 2015.

30. Barbi, M., C. Garcia-Pardo, A. Nevárez, V. P. Beltrán and N. Cardona, "UWB RSS-Based Localization for Capsule Endoscopy Using a Multilayer Phantom and In Vivo Measurements", *IEEE Transactions on Antennas and Propagation*, Vol. 67, No. 8, pp. 5035–5043, 2019.

31. Ye, Y., *Bounds on RF Cooperative Localization for Video Capsule Endoscopy*, Ph.D. Thesis, Worcester Polytechnic Institute, 2013.

32. Umay, I., B. Fidan and B. Barshan, "Localization and Tracking of Implantable Biomedical Sensors", *Sensors*, Vol. 17, No. 3, p. 583, 2017.

33. Worsøe, J., L. Fynne, T. Gregersen, V. Schlageter, L. A. Christensen, J. F. Dahlerup, N. J. M. Rijkhoff, S. Laurberg and K. Krogh, "Gastric Transit and Small Intestinal Transit Time and Motility Assessed by a Magnet Tracking System", *BMC Gastroenterology*, Vol. 11, p. 145, 2011.

34. Andrä, W., H. Danan, W. Kirmße, H.-H. Kramer, P. Saupe, R. Schmieg and M. E. Bellemann, "A Novel Method for Real-Time Magnetic Marker Monitoring in the Gastrointestinal Tract", *Physics in Medicine & Biology*, Vol. 45, No. 10, pp. 3081–3093, 2000.

35. Son, D., S. Yim and M. Sitti, "A 5-D Localization Method for a Magnetically Manipulated Untethered Robot Using a 2-D Array of Hall-Effect Sensors", *IEEE/ASME Transactions on Mechatronics*, Vol. 21, No. 2, pp. 708–716, 2016.

36. Pourhomayoun, M., Z. Jin and M. L. Fowler, "Accurate Localization of In-Body Medical Implants Based on Spatial Sparsity", *IEEE Transactions on Biomedical Engineering*, Vol. 61, No. 2, pp. 590–597, 2014.

37. Weitschies, W., H. Blume and H. Mönnikes, "Magnetic Marker Monitoring: High-

Resolution Real-Time Tracking of Oral Solid Dosage Forms in the Gastrointestinal Tract", *European Journal of Pharmaceutics and Biopharmaceutics*, Vol. 74, No. 1, pp. 93–101, 2010.

38. Huang, J., T. Mori, K. Takashima, S. Hashi and Y. Kitamura, "IM6D: Magnetic Tracking System with 6-DOF Passive Markers for Dexterous 3D Interaction and Motion", *ACM Transactions on Graphics*, Vol. 34, No. 6, p. 217, 2015.

39. Liu, L., C. Hu, W. Cai and M. Q.-H. Meng, "Capsule Endoscope Localization Based on Computer Vision Technique", *31st Annual International Conference of the IEEE Engineering in Medicine and Biology Society (EMBC)*, pp. 3711–3714, Minneapolis, Minnesota, USA, 2009.

40. Iakovidis, D. K., E. Spyrou, D. Diamantis and I. Tsiompanidis, "Capsule Endoscope Localization Based on Visual Features", *2013 IEEE 13th International Conference on Bioinformatics and Bioengineering (BIBE)*, pp. 1–4, Chania, Greece, 2013.

41. Iakovidis, D. K., G. Dimas, A. Karargyris, F. Bianchi, G. Ciuti and A. Koulaouzidis, "Deep Endoscopic Visual Measurements", *IEEE Journal of Biomedical and Health Informatics*, Vol. 23, No. 6, pp. 2211–2219, 2019.

42. Bao, G., *Body-SLAM: Simultaneous Localization and Mapping inside Human Body*, Ph.D. Thesis, Worcester Polytechnic Institute, 2014.

43. Oliveira, M., H. Araujo, I. N. Figueiredo, L. Pinto, E. Curto and L. Perdigoto, "Registration of Consecutive Frames From Wireless Capsule Endoscopy for 3D Motion Estimation", *IEEE Access*, Vol. 9, pp. 119533–119545, 2021.

44. Kalantar-zadeh, K., N. Ha, J. Z. Ou and K. J. Berean, "Ingestible Sensors", *ACS Sensors*, Vol. 2, No. 4, pp. 468–483, 2017.

45. Asci, C., R. Del-Rio-Ruiz, A. Sharma and S. Sonkusale, "Ingestible pH Sensing

Capsule with Thread-Based Electrochemical Sensors", *2022 IEEE Sensors*, pp. 1–4, Dallas, Texas, USA, 2022.

46. Cheng, C., Y. Wu, X. Li, Z. An, Y. Lu, F. Zhang, B. Su and Q. Liu, "A Wireless, Ingestible pH Sensing Capsule System Based on Iridium Oxide for Monitoring Gastrointestinal Health", *Sensors and Actuators: B. Chemical*, Vol. 349, p. 130781, 2021.

47. Curry, E. J., K. Ke, M. T. Chorsi, K. S. Wrobel, A. N. M. III, A. Patel, I. Kim, J. Feng, L. Yue, Q. Wu, C.-L. Kuo, K. W.-H. Lo, C. T. Laurencin, H. Ilies, P. K. Purohit and T. D. Nguyen, "Biodegradable Piezoelectric Force Sensor", *Proceedings of the National Academy of Sciences of the United States of America (PNAS)*, Vol. 115, No. 5, pp. 909–914, 2018.

48. Yu, K. J., D. Kuzum, S.-W. Hwang, B. H. Kim, H. Juul, N. H. Kim, S. M. Won, K. Chiang, M. Trumpis, A. G. Richardson, H. Cheng, H. Fang, M. Thomson, H. Bink, D. Talos, K. J. Seo, H. N. Lee, S.-K. Kang, J.-H. Kim, J. Y. Lee, Y. Huang, F. E. Jensen, M. A. Dichter, T. H. Lucas, J. Viventi, B. Litt and J. A. Rogers, "Bioresorbable Silicon Electronics for Transient Spatio-temporal Mapping of Electrical Activity from the Cerebral Cortex", *Nature Materials*, Vol. 15, No. 7, pp. 782–791, 2016.

49. Boutry, C. M., H. Chandrahalim, P. Streit, M. Schinhammer, A. C. Hänzi and C. Hierold, "Towards Biodegradable Wireless Implants", *Philosophical Transactions of the Royal Society A: Mathematical, Physical and Engineering Sciences*, Vol. 370, No. 1967, pp. 2418–2432, 2012.

50. Kang, S.-K., R. K. J. Murphy, S.-W. Hwang, S. M. Lee, D. V. Harburg, N. A. Krueger, J. Shin, P. Gamble, H. Cheng, S. Yu, Z. Liu, J. G. McCall, M. Stephen, H. Ying, J. Kim, G. Park, R. C. Webb, C. H. Lee, S. Chung, D. S. Wie, A. D. Gujar, B. Vemulapalli, A. H. Kim, K.-M. Lee, J. Cheng, Y. Huang, S. H. Lee, P. V. Braun, W. Z. Ray and J. A. Rogers, "Bioresorbable Silicon Electronic Sensors for

the Brain", *Nature*, Vol. 530, pp. 71–76, 2016.

51. Salvatore, G. A., J. Sülzle, F. D. Valle, G. Cantarella, F. Robotti, P. Jokic, S. Knobelspies, A. Daus, L. Büthe, L. Petti, N. Kirchgessner, R. Hopf, M. Magno and G. Tröster, "Biodegradable and Highly Deformable Temperature Sensors for the Internet of Things", *Advanced Functional Materials*, Vol. 27, No. 35, p. 1702390, 2017.

52. Boutry, C. M., Y. Kaizawa, B. C. Schroeder, A. Chortos, A. Legrand, Z. Wang, J. Chang, P. Fox and Z. Bao, "A Stretchable and Biodegradable Strain and Pressure Sensor for Orthopaedic Application", *Nature Electronics*, Vol. 1, pp. 314–321, 2018.

53. Boutry, C. M., A. Nguyen, Q. O. Lawal, A. Chortos, S. Rondeau-Gagné and Z. Bao, "A Sensitive and Biodegradable Pressure Sensor Array for Cardiovascular Monitoring", *Advanced Materials*, Vol. 27, No. 43, pp. 6954–6961, 2015.

54. Boutry, C. M., L. Beker, Y. Kaizawa, C. Vassos, H. Tran, A. C. Hinckley, R. Pfattner, S. Niu, J. Li, J. Claverie, Z. Wang, J. Chang, P. M. Fox and Z. Bao, "Biodegradable and Flexible Arterial-Pulse Sensor for the Wireless Monitoring of Blood Flow", *Nature Biomedical Engineering*, Vol. 3, No. 1, pp. 47–57, 2019.

55. Ararat, K., O. Altan, S. Serbest, O. Baser and S. Dumanli, "A Biodegradable Implant Antenna Detecting Post-Surgical Infection", *2020 14th European Conference on Antennas and Propagation (EuCAP)*, pp. 1–4, Copenhagen, Denmark, 2020.

56. Mani, G. K., K. Miyakoda, A. Saito, Y. Yasoda, K. Kajiwara, M. Kimura and K. Tsuchiya, "Microneedle pH Sensor: Direct, Label-Free, Real-Time Detection of Cerebrospinal Fluid and Bladder pH", *ACS Applied Materials Interfaces*, Vol. 9, No. 26, pp. 21651–21659, 2017.

57. Corsi, M., A. Paghi, S. Mariani, G. Golinelli, A. Debrassi, G. Egri, G. Leo, E. Vandini, A. Vilella, L. Dähne, D. Giuliani and G. Barillaro, "Bioresorbable Nanostructured Chemical Sensor for Monitoring of pH Level In Vivo", *Advanced Science*, Vol. 9, No. 22, p. 2202062, 2022.

58. Kwiatek, M. and J. Pandolfino, "The Bravo™ pH Capsule System", *Digestive and Liver Disease*, Vol. 40, No. 3, pp. 156–160, 2008.

59. Tran, K., R. Brun and B. Kuo, "Evaluation of Regional and Whole Gut Motility Using the Wireless Motility Capsule: Relevance in Clinical Practice", *Therapeutic Advances in Gastroenterology*, Vol. 5, No. 4, pp. 249–260, 2012.

60. Kalantar-Zadeh, K., K. J. Berean, N. Ha, A. F. Chrimes, K. Xu, D. Grando, J. Z. Ou, N. Pillai, J. L. Campbell, R. Brkljača, K. M. Taylor, R. E. Burgell, C. K. Yao, S. A. Ward, C. S. McSweeney, J. G. Muir and P. R. Gibson, "A Human Pilot Trial of Ingestible Electronic Capsules Capable of Sensing Different Gases in the Gut", *Nature Electronics*, Vol. 1, pp. 79–87, 2018.

61. Ashammakhi, N., A. L. Hernandez, B. D. Unluturk, S. A. Quintero, N. R. de Barros, E. H. Apu, A. B. Shams, S. Ostrovidov, J. Li, C. Contag, A. S. Gomes and M. Holgado, "Biodegradable Implantable Sensors: Materials Design, Fabrication, and Applications", *Advanced Functional Materials*, Vol. 31, No. 49, p. 2104149, 2021.

62. Santis, M. D. and I. Cacciotti, "Wireless Implantable and Biodegradable Sensors for Postsurgery Monitoring: Current Status and Future Perspectives", *Nanotechnology*, Vol. 31, No. 25, p. 252001, 2020.

63. Williams, D. F., "On the Mechanisms of Biocompatibility", *Biomaterials*, Vol. 29, No. 20, pp. 2941–2953, 2008.

64. Yin, L., X. Huang, H. Xu, Y. Zhang, J. Lam, J. Cheng and J. A. Rogers, "Mate-

rials, Designs, and Operational Characteristics for Fully Biodegradable Primary Batteries", *Advanced Materials*, Vol. 26, No. 23, pp. 3879–3884, 2014.

65. Yun, Y., Z. Dong, N. Lee, Y. Liu, D. Xue, X. Guo, J. Kuhlmann, A. Doepke, H. B. Halsall, W. Heineman, S. Sundaramurthy, M. J. Schulz, Z. Yin, V. Shanov, D. Hurd, P. Nagy, W. Li and C. Fox, "Revolutionizing Biodegradable Metals", *Materials Today*, Vol. 12, No. 10, pp. 22–32, 2009.

66. Sezer, N., Z. Evis, S. M. Kayhan, A. Tahmasebifar and M. Koç, "Review of Magnesium-Based Biomaterials and Their Applications", *Journal of Magnesium and Alloys*, Vol. 6, No. 1, pp. 23–43, 2018.

67. Luo, M., A. W. Martinez, C. Song, F. Herrault and M. G. Allen, "A Microfabricated Wireless RF Pressure Sensor Made Completely of Biodegradable Materials", *Journal of Microelectromechanical Systems*, Vol. 23, No. 1, pp. 4–13, 2014.

68. Hernandez, H. L., S.-K. Kang, O. P. Lee, S.-W. Hwang, J. A. Kaitz, B. Inci, C. W. Park, S. Chung, N. R. Sottos, J. S. Moore, J. A. Rogers and S. R. White, "Triggered Transience of Metastable Poly(phthalaldehyde) for Transient Electronics", *Advanced Materials*, Vol. 26, No. 45, pp. 7637–7642, 2014.

69. Heffernan, M. A. and E. J. O'Reilly, "Rapid Microwave-Assisted Synthesis and Characterisation of a Semiconducting Polymer With pKa Tuneable Degradation Properties", *European Polymer Journal*, Vol. 114, pp. 206–212, 2019.

70. Nair, L. S. and C. T. Laurencin, "Biodegradable Polymers as Biomaterials", *Progress in Polymer Science*, Vol. 32, No. 8–9, pp. 762–798, 2007.

71. Hosseini, E. S., S. Dervin, P. Ganguly, and R. Dahiya, "Biodegradable Materials for Sustainable Health Monitoring Devices", *ACS Applied Bio Materials*, Vol. 4, No. 1, pp. 163–194, 2021.

72. Li, C., C. Guo, V. Fitzpatrick, A. Ibrahim, M. J. Zwierstra, P. Hanna, A. Lechtig,

A. Nazarian, S. J. Lin and D. L. Kaplan, "Design of Biodegradable, Implantable Devices Towards Clinical Translation", *Nature Reviews Materials*, Vol. 5, pp. 61–81, 2020.

73. Prestwich, G. D. and S. Atzet, "Engineered Natural Materials", *Biomaterials Science*, chap. I.2.7, pp. 195–209, Elsevier, 2013.

74. Schmitt, E. E. and R. A. Polistina, "Polyglycolic Acid Prosthetic Devices", U. S. Patent 3463158A, August 26, 1969, `https://patents.google.com/patent/US3463158A/en`, accessed on July 08, 2024.

75. Schmitt, E. E., M. Epstein and R. A. Polistina, "Process for Polymerizing a Glycolide", U. S. Patent 3442871A, May 06, 1969, `https://patents.google.com/patent/US3442871A/en`, accessed on July 08, 2024.

76. Middleton, J. C. and A. J. Tipton, "Synthetic Biodegradable Polymers as Orthopedic Devices", *Biomaterials*, Vol. 21, No. 23, pp. 2335–2346, 2000.

77. Vroman, I. and L. Tighzert, "Biodegradable Polymers", *Materials*, Vol. 2, No. 2, pp. 307–344, 2009.

78. Tian, H., Z. Tang, X. Zhuang, X. Chen and X. Jing, "Biodegradable Synthetic Polymers: Preparation, Functionalization, and Biomedical Application", *Progress in Polymer Science*, Vol. 37, No. 2, pp. 237–280, 2012.

79. Huang, X., D. Wang, Z. Yuan, W. Xie, Y. Wu, R. Li, Y. Zhao, D. Luo, L. Cen, B. Chen, H. Wu, H. Xu, X. Sheng, M. Zhang, L. Zhao and L. Yin, "A Fully Biodegradable Battery for Self-Powered Transient Implants", *Small*, Vol. 14, No. 28, p. e1800994, 2018.

80. Lü, J.-M., X. Wang, C. Marin-Muller, H. Wang, P. H. Lin, Q. Yao and C. Chen,

"Current Advances in Research and Clinical Applications of PLGA-Based Nanotechnology", *Expert Review of Molecular Diagnostics*, Vol. 9, No. 4, pp. 325–341, 2009.

81. Hwang, S., C. H. Lee, H. Cheng, J. Jeong, S.-K. Kang, J.-H. Kim, J. Shin, J. Yang, Z. Liu, G. A. Ameer, Y. Huang and J. A. Rogers, "Biodegradable Elastomers and Silicon Nanomembranes/Nanoribbons for Stretchable, Transient Electronics and Biosensors", *Nano Letters*, Vol. 15, No. 5, pp. 2801–2808, 2015.

82. Pal, R. K., A. A. Farghaly, C. Wang, M. M. Collinson, S. C. Kundu and V. K. Yadavalli, "Conducting Polymer-Silk Biocomposites for Flexible and Biodegradable Electrochemical Sensors", *Biosensors and Bioelectronic*, Vol. 81, pp. 294–302, 2016.

83. Kaur, G., R. Adhikari, P. Cass, M. Bown and P. Gunatillake, "Electrically Conductive Polymers and Composites for Biomedical Applications", *RSC Advances*, Vol. 5, pp. 37553–37567, 2015.

84. Balint, R., N. J. Cassidy and S. H. Cartmell, "Conductive Polymers: Towards a Smart Biomaterial for Tissue Engineering", *Acta Biomaterialia*, Vol. 10, No. 6, pp. 2341–2353, 2014.

85. Lanzani, G., "Materials for Bioelectronics: Organic Electronics Meets Biology", *Nature Materials*, Vol. 13, pp. 775–776, 2014.

86. Owens, R. M. and G. G. Malliaras, "Organic Electronics at the Interface with Biology", *MRS Bulletin*, Vol. 35, No. 6, pp. 449–456, 2010.

87. Tong, W. Y., M. J. Sweetman, E. R. Marzouk, C. Fraser, T. Kuchel and N. H. Voelcker, "Towards a Subcutaneous Optical Biosensor Based on Thermally Hydrocarbonised Porous Silicon", *Biomaterials*, Vol. 74, pp. 217–230, 2016.

88. He, Y., C. Fan and S.-T. Lee, "Silicon Nanostructures for Bioapplications", *Nano*

Today, Vol. 5, No. 4, pp. 282–295, 2010.

89. Alpuim, P., V. Correia, E. Marins, J. Rocha, I. Trindade and S. Lanceros-Mendez, "Piezoresistive Silicon Thin Film Sensor Array for Biomedical Applications", *Thin Solid Films*, Vol. 519, No. 14, pp. 4574–4577, 2011.

90. Chang, J.-K., H. Fang, C. A. Bower, E. Song, X. Yu and J. A. Rogers, "Materials and Processing Approaches for Foundry-Compatible Transient Electronics", *Proceedings of the National Academy of Sciences of the United States of America (PNAS)*, Vol. 114, No. 28, pp. E5522–E5529, 2017.

91. Shin, J., Y. Yan, W. Bai, Y. Xue, P. Gamble, L. Tian, I. Kandela, C. R. Haney, W. Spees, Y. Lee, M. Choi, J. Ko, H. Ryu, J.-K. Chang, M. Pezhouh, S.-K. Kang, S. M. Won, K. J. Yu, J. Zhao, Y. K. Lee, M. R. MacEwan, S.-K. Song, Y. Huang, W. Z. Ray and J. A. Rogers, "Bioresorbable Pressure Sensors Protected With Thermally Grown Silicon Dioxide for the Monitoring of Chronic Diseases and Healing Processes", *Nature Biomedical Engineering*, Vol. 3, pp. 37–46, 2019.

92. Park, J.-H., L. Gu, G. von Maltzahn, E. Ruoslahti, S. N. Bhatia and M. J. Sailor, "Biodegradable Luminescent Porous Silicon Nanoparticles for In Vivo Applications", *Nature Materials*, Vol. 8, No. 4, pp. 331–336, 2009.

93. Acquaroli, L. N., T. Kuchel and N. H. Voelcker, "Towards Implantable Porous Silicon Biosensors", *RSC Advances*, Vol. 4, pp. 34768–34773, 2014.

94. Cil, E., I. V. Soares, D. Renaudeau, R. Lucas, S. Dumanli, R. Sauleau and D. Nikolayev, "On the Use of Impedance Detuning for Gastrointestinal Segment Tracking of Ingestible Capsules", *IEEE Transactions on Antennas and Propagation*, Vol. 71, No. 2, pp. 1977–1981, 2023.

95. Smith, M. S., "Properties of Dielectrically Loaded Antennas", *Proc. IEE*, Vol. 124, No. 10, pp. 837–839, 1977.

96. Chen, W. K., *The Electrical Engineering Handbook*, Elsevier Academic Press, Boston, 2005.

97. Olaode, O. O., W. D. Palmer and W. T. Joines, "Effects of Meandering on Dipole Antenna Resonant Frequency", *IEEE Antennas and Wireless Propagation Letters*, Vol. 11, pp. 122–125, 2012.

98. Brown, R. G., R. A. Sharpe, W. L. Hughes and R. E. Post, *Lines, Waves, and Antennas*, John Wiley & Sons, Inc., New York, 2nd edn., 1973.

99. Endo, T., Y. Sunahara, S. Satoh and T. Katagi, "Resonant Frequency and Radiation Efficiency of Meander Line Antennas", *Electronics and Communications in Japan, Part 2*, Vol. 83, No. 1, pp. 52–58, 2000.

100. Puente, D., D. Valderas, J. García, J. Meleéndez, J. Gómez and J. I. Sancho, "Resonant Frequency Calculation of Meander Dipole Antennas by TLM", *Microwave and Optical Technology Letters*, Vol. 50, No. 6, pp. 1707–1712, 2008.

101. Nikolayev, D., M. Zhadobov, P. Karban and R. Sauleau, "Conformal Antennas for Miniature In-Body Devices: The Quest to Improve Radiation Performance", *Radio Science Bulletin*, Vol. 2017, No. 363, pp. 52–64, 2017.

102. Izdebski, P. M., H. Rajagopalan and Y. Rahmat-Samii, "Conformal Ingestible Capsule Antenna: A Novel Chandelier Meandered Design", *IEEE Transactions on Antennas and Propagation*, Vol. 57, No. 4, pp. 900–909, 2009.

103. Cil, E., S. Dumanli and D. Nikolayev, "Examination of Impedance Response of Capsule-Integrated Antennas Through Gastrointestinal Tract", *2022 16th European Conference on Antennas and Propagation (EuCAP)*, pp. 1–5, Madrid, Spain, 2022.

104. Nikam, A., P. R. Sahoo, S. Musale, R. R. Pagar, A. C. Paiva-Santos and P. S. Giram, "A Systematic Overview of Eudragit® Based Copolymer for Smart Health-

care", *Pharmaceutics*, Vol. 15, No. 2, p. 587, 2023.

105. ANSYS, "ANSYS High Frequency Structure Simulator", `https://www.ansys.com/products/electronics/ansys-hfss`, accessed on September, 2022.

106. IT'IS Foundation, "It'Is Tissue Properties Database", `https://itis.swiss/virtual-population/tissue-properties/database`, accessed on October, 2023.

107. Balanis, C. A., *Antenna Theory: Analysis and Design*, John Wiley & Sons, Inc., Hoboken, New Jersey, 4th edn., 2016.

APPENDIX A: DIPOLE ANTENNA

Wire antennas are among the oldest, simplest, and most cost-effective types of antennas, providing considerable versatility across a wide range of applications [107]. The dipole equations will be given for a finite length dipole as in [107].

For a very thin dipole ($a < \lambda/50$), the current distribution can be approximated by,

$$\mathbf{I}_e(x'=0, y'=0, z') = \begin{cases} \hat{\mathbf{a}}_z I_0 \sin\left[k\left(\frac{l}{2} - z'\right)\right], & 0 \le z' \le l/2, \\ \hat{\mathbf{a}}_z I_0 \sin\left[k\left(\frac{l}{2} + z'\right)\right], & -l/2 \le z' \le 0. \end{cases} \tag{A.1}$$

This current distribution assumes an infinitesimal dipole, with the current diminishing to zero at the two ends ($z' = \pm l/2$). It has been experimentally confirmed that in a centrally fed wire antenna the current distribution is sinusoidal. The null points stand at the ends. For $l = \lambda/2$, the current distribution described by Equation (A.1) is illustrated in Figure A.1. The antenna's geometry is illustrated in Figure A.2.

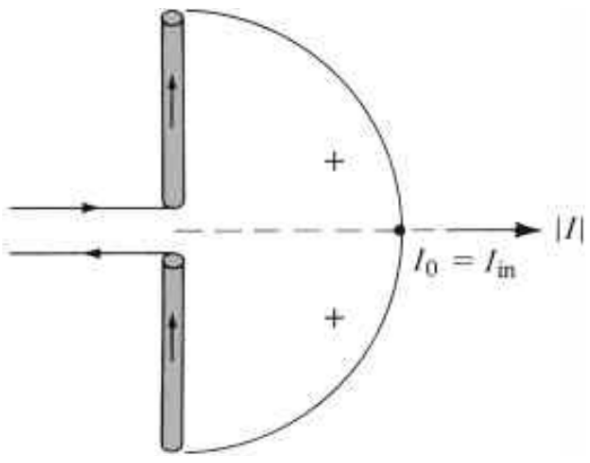

Figure A.1. Current distribution for a center-fed dipole antenna with length $l = \lambda/2$. Reproduced with licensed permission from "John Wiley and Sons", publisher of [107].

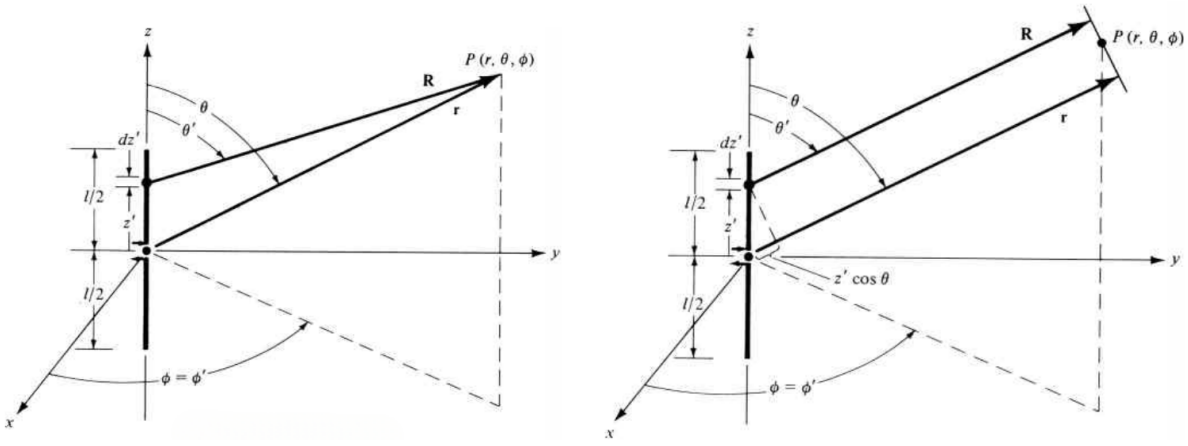

(a) (b)

Figure A.2. Center-fed dipole antenna with length $l = \lambda/2$; a: Finite dipole geometry, b: Far-field approximations. Reproduced with licensed permission from the "John Wiley and Sons", publisher of [107].

The antenna in Figure A.2 can be divided into many tiny segments, each with a length of $\Delta z'$. As we increase the number of these subdivisions, each tiny segment becomes an infinitesimal dipole with a length of dz'. For an infinitesimal dipole with length dz' that is located along the z-axis at z', we can determine the far-field electric and magnetic field components using Equation (A.2), as follows,

$$\begin{aligned} E_\theta &\simeq j\eta \frac{kI_0 l e^{-jkr}}{4\pi r} \sin\theta, \\ E_r &\simeq E_\phi = H_r = H_\theta = 0, \\ H_\phi &\simeq j \frac{kI_0 l e^{-jkr}}{4\pi r} \sin\theta, \end{aligned} \tag{A.2}$$

$$dE_\theta \simeq jn \frac{kI_e(x', y', z') e^{-jkR}}{4\pi R} \sin\theta \, dz', \tag{A.3}$$

$$dE_r \simeq dE_\phi = dH_\theta = 0, \tag{A.4}$$

$$dH_\phi \simeq j \frac{kI_e(x', y', z') e^{-jkR}}{4\pi R} \sin\theta \, dz'. \tag{A.5}$$

Where R is given by (A.6) and (A.7), as also depicted in Figure A.2,

$$R = \sqrt{(x - x')^2 + (y - y')^2 + (z - z')^2} = \sqrt{x^2 + y^2 + (z - z')^2}, \tag{A.6}$$

or

$$R = \sqrt{(x^2 + y^2 + z^2) + (-2zz' + z'^2)} = \sqrt{r^2 + (-2rz' \cos\theta + z'^2)}. \tag{A.7}$$

Using the far-field approximations given by (A.8), (A.3) turns into (A.9) as folllows,

$$\begin{aligned} R &\simeq r - z'\cos\theta, \qquad \text{(for phase terms)}, \\ R &\simeq r, \qquad\qquad\ \ \text{(for amplitude terms)}, \end{aligned} \tag{A.8}$$

$$dE_\theta \simeq jn\frac{kI_e(x',y',z')e^{-jkr}}{4\pi r}\sin\theta e^{jkz'\cos\theta}\,dz'. \tag{A.9}$$

After integration over all the infinitesimal elements, we have,

$$E_\theta = \int_{-l/2}^{+l/2} dE_\theta = jn\frac{ke^{-jkr}}{4\pi r}\sin\theta\left[\int_{-l/2}^{+l/2} I_e(x',y',z')e^{jkz'\cos\theta}\,dz'\right]. \tag{A.10}$$

We know that the overall field of the antenna is equivalent to the product of the element and space factors, as follows,

$$\text{total field} = (\text{element factor}) \times (\text{space factor}). \tag{A.11}$$

For the current distribution of (A.1), (A.10) is,

$$\begin{aligned} E_\theta \simeq jn\frac{kI_0e^{-jkr}}{4\pi r}\sin\theta\Bigg\{&\int_{-l/2}^{0}\sin\left[k\left(\frac{l}{2}+z'\right)\right]e^{jkz'\cos\theta}\,dz' \\ &+\int_{0}^{+l/2}\sin\left[k\left(\frac{l}{2}-z'\right)\right]e^{jkz'\cos\theta}\,dz'\Bigg\}. \end{aligned} \tag{A.12}$$

Each integral in (A.12) is integrated utilizing,

$$\int e^{\alpha x}\sin(\beta x+\gamma)\,dx = \frac{e^{\alpha x}}{\alpha^2+\beta^2}[\alpha\sin(\beta x+\gamma)-\beta\cos(\beta x+\gamma)], \tag{A.13}$$

where,

$$\begin{aligned} \alpha &= \pm jk\cos\theta, \\ \beta &= \pm k, \\ \gamma &= kl/2. \end{aligned} \tag{A.14}$$

At this point, some mathematical manipulations are required, but they are omitted as they fall beyond the scope of this work. After that, (A.12) becomes,

$$E_\theta \simeq jn\frac{I_0e^{-jkr}}{2\pi r}\left[\frac{\cos\left(\frac{kl}{2}\cos\theta\right)-\cos\left(\frac{kl}{2}\right)}{\sin\theta}\right]. \tag{A.15}$$

Using a similar approach, or by considering the relationship between the E_θ and H_ϕ in the far field as given by (A.16) or (A.17), the total H_ϕ component is calculated.

The ratio of E_θ to H_ϕ is equal to,

$$Z_w = \frac{E_\theta}{H_\phi} \simeq \eta, \tag{A.16}$$

where,

$$Z_w = \text{wave impedance},$$

η = intrinsic impedance ($377 \simeq 120\pi$ ohms for free-space).

$$\begin{aligned} H_r &\simeq 0, \\ H_\theta &= -\frac{E_\phi}{\eta}, \\ H_\phi &\simeq +\frac{E_\theta}{\eta}. \end{aligned} \tag{A.17}$$

$$H_\phi \simeq \frac{E_\theta}{\eta} \simeq j\frac{I_0 e^{-jkr}}{2\pi r}\left[\frac{\cos\left(\frac{kl}{2}\cos\theta\right) - \cos\left(\frac{kl}{2}\right)}{\sin\theta}\right], \tag{A.18}$$

In our case, the average Poynting vector is,

$$\mathbf{W}_{av} = \frac{1}{2}\Re[\mathbf{E}\times\mathbf{H}^*] = \frac{1}{2}\Re[\hat{\mathbf{a}}_\theta E_\theta \times \hat{\mathbf{a}}_\phi H_\phi^*] = \frac{1}{2}\Re\left[\hat{\mathbf{a}}_\theta E_\theta \times \frac{\hat{\mathbf{a}}_\phi E_\theta^*}{\eta}\right], \tag{A.19}$$

or

$$\mathbf{W}_{av} = \hat{\mathbf{a}}_r W_{av} = \hat{\mathbf{a}}_r \frac{1}{2\eta}|E_\theta|^2 = \hat{\mathbf{a}}_r \eta \frac{|I_0|^2}{8\pi^2 r^2}\left[\frac{\cos\left(\frac{kl}{2}\cos\theta\right) - \cos\left(\frac{kl}{2}\right)}{\sin\theta}\right]^2. \tag{A.20}$$

Thus the radiation intensity is,

$$U = r^2 W_{av} = \eta\frac{|I_0|^2}{8\pi^2}\left[\frac{\cos\left(\frac{kl}{2}\cos\theta\right) - \cos\left(\frac{kl}{2}\right)}{\sin\theta}\right]^2. \tag{A.21}$$

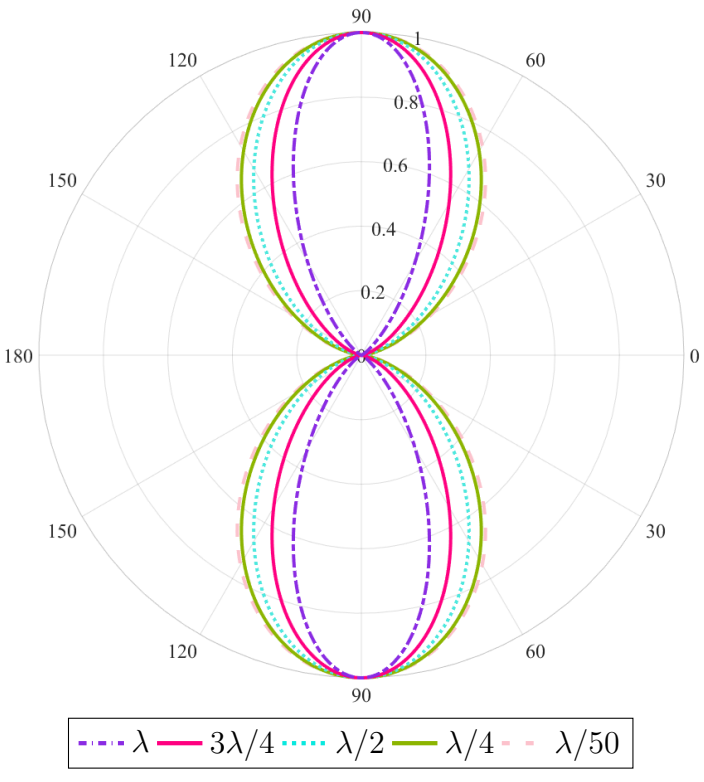

Figure A.3. The normalized elevation power patterns, for $l = \lambda/50, \lambda/4, \lambda/2, 3\lambda/4,$ and λ.

The normalized power patterns in the elevation plane, as given by (A.21) for $l = \lambda/4, \lambda/2, 3\lambda/4, \lambda$ and $\lambda/50$ are shown plotted in Figure A.3. Increasing the length of the antenna results in a narrower beam. Due to this fact, the directivity also increases with length.

When the length of a dipole exceeds one wavelength ($l > \lambda$), the number of lobes in the radiation pattern increases. Figure A.4 shows the normalized power pattern for a dipole with $l = 1.25\lambda$. To highlight variations in the elevation plane directional pattern, a 90° angular section has been omitted.

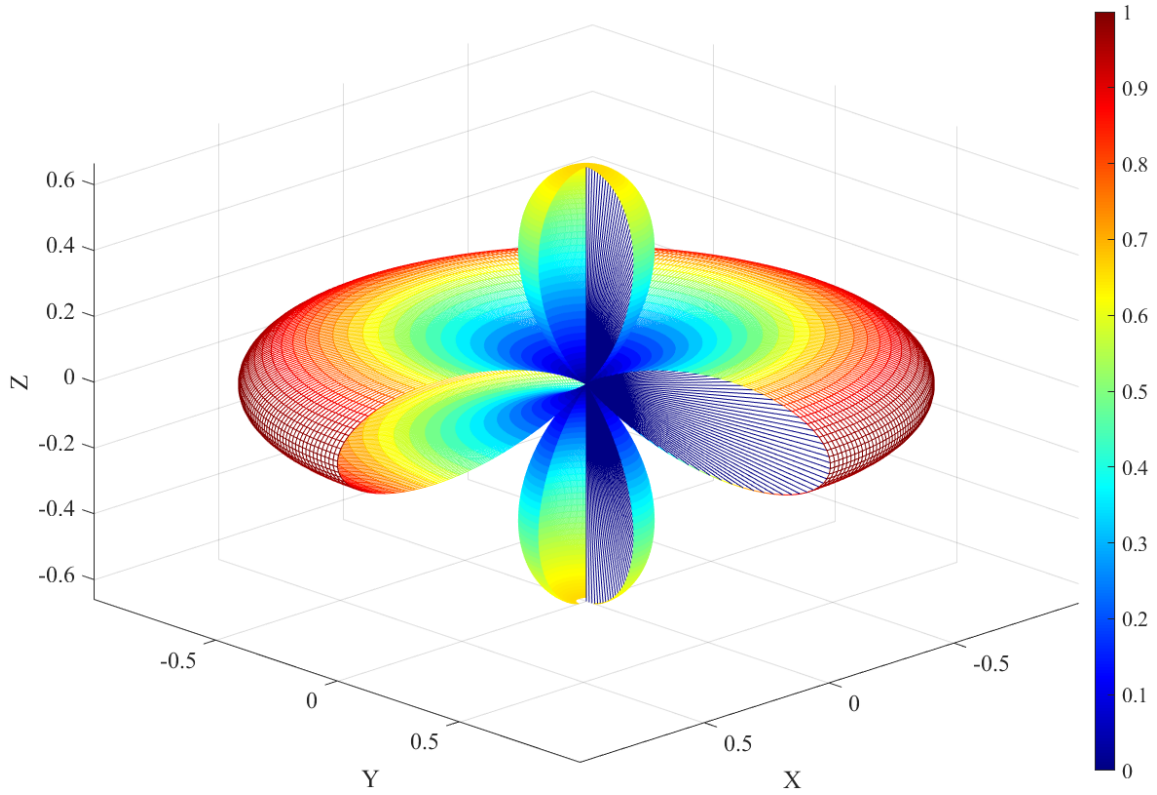

Figure A.4. Normalized power pattern for a dipole antenna with length $l = 1.25\lambda$; a 90° angular section has been omitted.

The average Poynting vector of (A.20) is integrated over a sphere with radius r. Thus,

$$P_{rad} = \iint_S \mathbf{W_{av}} \cdot d\mathbf{s} = \int_0^{2\pi} \int_0^{\pi} \hat{\mathbf{a}}_r W_{av} \cdot \hat{\mathbf{a}}_r r^2 \sin\theta \, d\theta \, d\phi = \int_0^{2\pi} \int_0^{\pi} W_{av} r^2 \sin\theta \, d\theta \, d\phi. \tag{A.22}$$

Using (A.20), (A.22) becomes,

$$P_{rad} = \int_0^{2\pi} \int_0^{\pi} W_{av} r^2 \sin\theta \, d\theta \, d\phi = \eta \frac{|I_0|^2}{4\pi} \int_0^{\pi} \left[\frac{\cos\left(\frac{kl}{2}\cos\theta\right) - \cos\left(\frac{kl}{2}\right)}{\sin\theta} \right]^2 d\theta. \quad \text{(A.23)}$$

As a result of some mathematical manipulations, (A.23) becomes,

$$\begin{aligned} P_{rad} = \eta \frac{|I_0|^2}{4\pi} \Bigg\{ & C + \ln(kl) - C_i(kl) + \frac{1}{2}\sin(kl)[S_i(2kl) - 2S_i(kl)] \\ & + \frac{1}{2}\cos(kl)[C + \ln(kl/2) + C_i(2kl) - 2C_i(kl)] \Bigg\}, \end{aligned} \quad \text{(A.24)}$$

where $C = 0.5772$ (Euler's constant) and $C_i(x)$ and $S_i(x)$ are the cosine and sine integrals [107] given by,

$$C_i(x) = -\int_x^{\infty} \frac{\cos y}{y} dy = \int_{-\infty}^{x} \frac{\cos y}{y} dy, \quad \text{(A.25)}$$

$$S_i(x) = \int_0^{x} \frac{\sin y}{y} dy. \quad \text{(A.26)}$$

We can obtain the radiation resistance using (A.27) and (A.24) can be written as (A.28),

$$P_{\text{rad}} = \eta \left(\frac{\pi}{3}\right) \left| \frac{I_0 l}{\lambda} \right|^2 = \frac{1}{2}|I_0|^2 R_r. \quad \text{(A.27)}$$

$$\begin{aligned} R_r = \frac{2P_{rad}}{|I_0|^2} = \eta \frac{1}{2\pi} \Bigg\{ & C + \ln(kl) - C_i(kl) + \frac{1}{2}\sin(kl) \times [S_i(2kl) - 2S_i(kl)] \\ & + \frac{1}{2}\cos(kl) \times [C + \ln(kl/2) + C_i(2kl) - 2C_i(kl)] \Bigg\}. \end{aligned} \quad \text{(A.28)}$$

Using the EMF method [107], the imaginary portion of the impedance, *with respect to the current peak*, is given by,

$$\begin{aligned} X_m = \frac{\eta}{4\pi} \Bigg\{ & 2S_i(kl) + \cos(kl)\,[2S_i(kl) - S_i(2kl)] \\ & - \sin(kl) \left[2C_i(kl) - C_i(2kl) - C_i\left(\frac{2ka^2}{l}\right) \right] \Bigg\}. \end{aligned} \quad \text{(A.29)}$$

In theory, the wire radius does not impact the input resistance, as shown by Equation (A.28). However, in practice, the wire radius does influence the input resistance, though its impact is less significant compared to its effect on the input reactance.

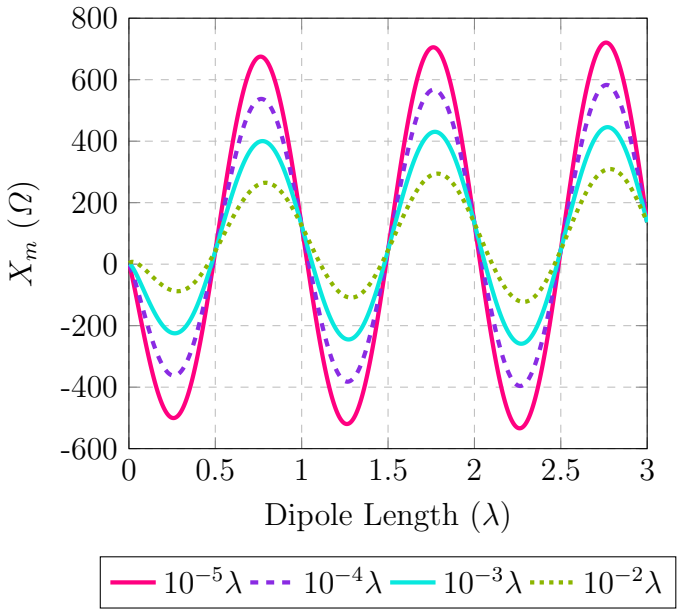

Figure A.5. Reactance of a thin dipole with sinusoidal current distribution for $a = 10^{-5}\lambda$, $a = 10^{-4}\lambda$, $a = 10^{-3}\lambda$ and $a = 10^{-2}\lambda$, a is the wire radius.

As shown in Figure 3.3, a dipole antenna's radiation pattern becomes more directional With an increase in length. When the length exceeds one wavelength, the pattern develops additional lobes, which results in decreased directivity. Directivity, a measure of the antenna's directional performance, is defined as follows:

$$D_0 = 4\pi \frac{[F(\theta,\phi)]_{\max}}{\int_0^{2\pi}\int_0^{\pi} F(\theta,\phi)\sin\theta\, d\theta\, d\phi}, \tag{A.30}$$

where

$$U = B_0 F(\theta,\phi), \tag{A.31}$$

From (A.21), the dipole antenna of length l has

$$F(\theta,\phi) = F(\theta) = \left[\frac{\cos\left(\frac{kl}{2}\cos\theta\right) - \cos\left(\frac{kl}{2}\right)}{\sin\theta}\right]^2, \tag{A.32}$$

and,

$$B_0 = \eta\frac{|I_0|^2}{8\pi^2}. \tag{A.33}$$

Since the pattern does not depend on ϕ, (A.30) reduces to

$$D_0 = \frac{2[F(\theta)]_{\max}}{\int_0^{\pi} F(\theta)\sin\theta\, d\theta}. \tag{A.34}$$

Equation (A.34) can be written, using (A.23), (A.24), and (A.33), as

$$D_0 = \frac{2[F(\theta)]_{\max}}{Q}, \tag{A.35}$$

where

$$Q = \Big\{ C + \ln(kl) - C_i(kl) + \frac{1}{2}\sin(kl)[S_i(2kl) - 2S_i(kl)] + \frac{1}{2}\cos(kl)[C + \ln(kl/2) + C_i(2kl) - 2C_i(kl)] \Big\}. \quad \text{(A.36)}$$

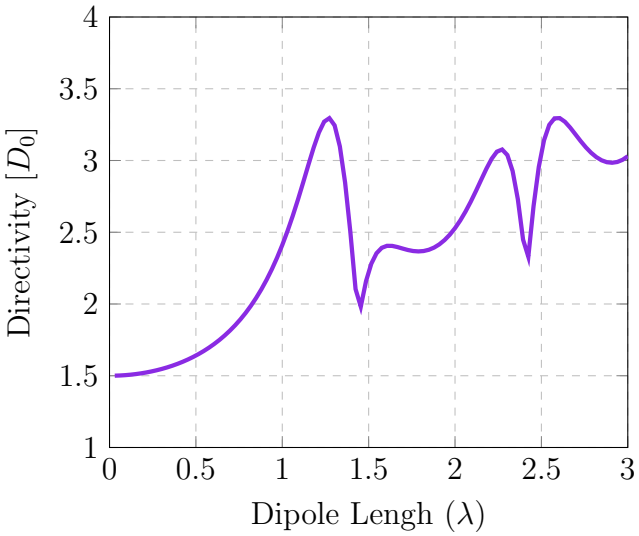

Figure A.6. Directivity.

The input impedance of an antenna is defined as "the ratio of voltage to current at a pair of terminals or the ratio of the relevant components of the electric to magnetic fields at a specific point." The real part of this impedance, known as the input resistance, corresponds to the radiation resistance for a lossless antenna. This radiation resistance represents the power radiated as real power [107].

For a dipole with a length l and a sinusoidal current distribution as defined in (A.1), the radiation resistance is given by (A.28). Notably, this radiation resistance is measured at the current peak, which, for certain lengths ($l = \lambda/4, 3\lambda/4, \lambda$, etc.), does not coincide with the input terminals of the antenna. To align the radiation resistance with the input terminals, the antenna is first considered lossless ($R_L = 0$). Subsequently, the input terminal power is equated to the power at the point of maximum current.

$$\frac{|I_{in}|^2}{2} R_{in} = \frac{|I_0|^2}{2} R_r, \quad \text{(A.37)}$$

or

$$R_{in} = \left(\frac{I_0}{I_{in}}\right)^2 R_r, \tag{A.38}$$

where,

R_{in} = radiation resistance at input (feed) terminals,

R_r = radiation resistance at current maximum,

I_0 = current maximum,

I_{in} = current at input terminals.

For a dipole of length l, the current at the input terminals (I_{in}) is related to the current maximum (I_0). Also, referring to Figure A.7 by,

$$I_{in} = I_0 \sin\left(\frac{kl}{2}\right). \tag{A.39}$$

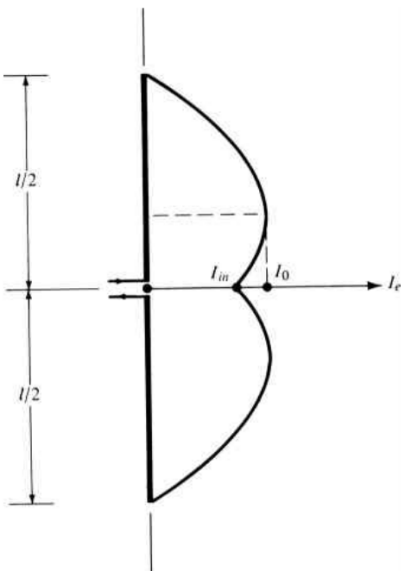

Figure A.7. The distribution of current in a linear wire antenna when the maximum current is not at the input terminals. Reproduced with licensed permission from "John Wiley and Sons", publisher of [107].

Thus the input radiation resistance of (A.38) can be written as

$$R_{in} = \frac{R_r}{\sin^2\left(\frac{kl}{2}\right)}. \tag{A.40}$$

Values of R_{in} for $0 < l \leq 3\lambda$ are shown in Figure A.8.

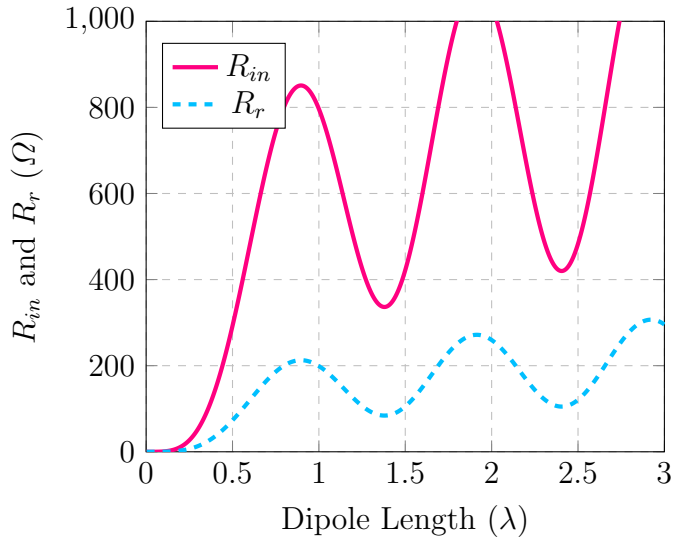

Figure A.8. Radiation resistance and input resistance of a thin dipole with sinusoidal current distribution.

When the full length of the antenna is a multiple of λ (i.e., $l = n\lambda, n = 1, 2, 3, \ldots$), it is apparent from (A.16) that $I_{in} = 0$. That is,

$$I_{in} = I_0 \sin\left[k\left(\frac{l}{2} + z'\right)\right]_{z'=0} = I_0 \sin\left(\frac{kl}{2}\right) = 0, \quad n = 1, 2, 3, \ldots. \tag{A.41}$$

which reveals that the radiation resistance at the input terminals, as specified by (A.38) or (A.40), is theoretically infinite. In practical terms, this doesn't hold true because the current distribution deviates from a purely sinusoidal form, particularly at the feeding location. However, it still exhibits very high values. Two major factors contributing to the non-sinusoidal current distribution on an actual wire antenna are the nonzero radius of the wire and the finite gap spacing at the terminals.

According to equations (A.28) and (A.40), the radiation resistance and input resistance are calculated using the ideal current distribution from equation (A.1) and do not take into account the finite radius of the wire or the gap spacing at the feed. Although the radius of the wire has a negligible effect on the resistances, the feed gap spacing plays a crucial role, especially when the current is minimal at or near the feed point.

To analytically address the presence of nonzero current at the feed point in antennas with a finite gap at their terminals, Schelkunoff and Friis [107] modified the current distribution of (A.1) by factoring in a quadrature term. This additional term accounts for the impact of radiation on the distribution of current in the antenna. To put it another way, once the antenna is stimulated by the 'ideal' current distribution of (A.1), the generated electric and magnetic fields disturb this ideal distribution. This interaction is included by modifying (A.1) to,

$$\mathbf{I}_e(x',y',z') = \begin{cases} \hat{\mathbf{a}}_z \left\{ I_0 \sin\left[k\left(\frac{l}{2}-z'\right)\right] + jpI_0\left[\cos(kz') - \cos\left(\frac{kl}{2}\right)\right]\right\}, & 0 \le z' \le l/2, \\ \hat{\mathbf{a}}_z \left\{ I_0 \sin\left[k\left(\frac{l}{2}+z'\right)\right] + jpI_0\left[\cos(kz') - \cos\left(\frac{kl}{2}\right)\right]\right\}, & -l/2 \le z' \le 0. \end{cases} \tag{A.42}$$

When $l = \lambda/2$,

$$\mathbf{I}_e(x',y',z') = \hat{\mathbf{a}}_z I_0(1+jp)\cos(kz'), \quad 0 \le z' \le \lambda/4, \tag{A.43}$$

and for $l = \lambda$,

$$\mathbf{I}_e(x',y',z') = \begin{cases} \hat{\mathbf{a}}_z I_0\left[\sin(kz') + jp\left(1+\cos(kz')\right)\right], & 0 \le z' \le \lambda/2, \\ \hat{\mathbf{a}}_z I_0\left[-\sin(kz') + jp\left(1+\cos(kz')\right)\right], & -\lambda/2 \le z' \le 0. \end{cases} \tag{A.44}$$

Hence, for $l = \lambda/2$ the shape of the current distribution remains unchanged while for $l = \lambda$ it is altered by the second term which is the dominant term for small values of z'.

APPENDIX B: COPYRIGHT PERMISSION

Figure A.1, Figure A.2 and Figure A.7 have been sourced from [107]. Licensed permission for their inclusion has been granted by "John Wiley and Sons", the publisher of [107] under the licence number 5853220494431.

APPENDIX C: USE OF PRODUCTIVE ARTIFICIAL INTELLIGENCE

In this thesis, ChatGPT developed by OpenAI was used for language refinement, text editing and image generation.